Ornithopter flight dynamics: Measurement and analysis of the Robird's flapping wing

S.H. (Steven) Gies

MSc Report

Committee:
Prof.dr.ir. S. Stramigioli
Dr.ir. G.A. Folkertsma
Prof.dr.ir. C.H. Venner

October 2017

048RAM2017
Robotics and Mechatronics
EE-Math-CS
University of Twente
P.O. Box 217
7500 AE Enschede
The Netherlands

Ornithopter Flight Dynamics: Measurement and Analysis of the Robird's Flapping Wing

S.H. Gies[1], G.A. Folkertsma[1,2], S. Stramigioli[1], C.H. Venner[3].

***Abstract*— A mechatronic setup is used to study the flight dynamics of an ornithopter in a wind tunnel. The amount of pitching, flapping frequency and wind speed can be controlled individually and their influence on a flexible wing are analyzed through a series of experiments. A stereo vision setup and corresponding tracking algorithm are used to create a digital reconstruction of the wing's 3D motion. In addition, force, power and efficiency measurements were performed and particle image velocimetry was used to determine the effects of the wing on the air flow. The resulting dataset forms a basis for research on ornithopter flight and biomimetics, as well as further development of robotic birds and aerodynamical models. For the setup considered here, results showed that in order to optimize the generation of thrust, the amount of twisting of the wing should decrease as air speed increases. The stereo vision measurements revealed that wind speed dominated pitching angles and consequently angle of attack due to the wing's flexibility.**

I. INTRODUCTION

A. Robird

The Robird (Figure 1) is a flying robot developed by Clear Flight Solutions[2] in collaboration with research group RaM[1]. Unlike many other drones, the Robird is specifically aimed at imitating a real bird and therefore uses flapping wings to fly. Due to its close resemblance to a bird of prey, the Robird can be used to scare off pest birds, for example at airports or agricultural areas. Despite the fact that controlled and stable flight has been achieved already, the understanding of its exact flight dynamics is limited. It is known that lift and thrust forces generated by the flapping wing depend on a large number of parameters, including air velocity and flapping frequency.

The actuation of the wings is performed by two motors, each connected to a driving rod, together forming the skeleton of the wing. By introducing a phase difference γ between the two heaving motions, the wing gets twisted along its span and additional pitching is generated. This is believed to contribute to an improved flight performance as it effectively determines the angle of attack. The influences of other parameters, such as (the amplitude of) the motion profile and the amount of flexing and twisting are still largely unknown.

B. Research goals

Previously, a set-up has been built that allows for the actuation of a single flapping wing for testing purposes [1][2]. Tests can for example include tuning of flapping frequency, mechanically induced pitching or the performance of entire wing designs. In the past, the set-up has been used to gather valuable data such as 6-DOF force measurements [1] and even stereo vision footage [3]. However, until now the application of these measurements has remained limited. A reason for this is that the various measurements were performed separately with different wing models and control settings, which means that they could not be correlated with each other. The aim of this research is therefore the **acquisition, synchronization, processing and analysis** of a complete set of measurements during wind tunnel experiments. The results may prove to be a great contribution towards the following sub-goals:

1) Digitizing the flexible behaviour of the wing under various circumstances: In particular, the influence of pitch control and wind speed are of interest. The results can be used to verify behaviour (i.e. whether the driving rods induce twisting of the wing as expected), or to develop new wings in the future. Previous research has pointed out that flapping wing propulsion is greatly affected by the wing's stiffness [4]. Furthermore, this will aid the development of aerodynamic models of the Robird as these currently mainly rely on qualitative, basic theory instead of quantitative measurements.

2) Optimization of actuation parameters: Previous research performed on airfoils poses the hypothesis that thrust, lift and efficiency of a flapping wing strongly depend on flapping frequency, pitch and air speed. In particular, it is expected that, for the production of thrust, the optimal degree of pitching decreases with air speed [5][6]. This hypothesis is supported by reality: real birds use long hauls with high pitching when taking off, compared to only slight wing motion when cruising at high speed. Previous research also revealed that flight efficiency of ornithopters peaks for

Fig. 1. The Robird: peregrine falcon model.

[1] Robotics and Mechatronics Group, CTIT institute, University of Twente, Enschede, The Netherlands

[2]Clear Flight Solutions, Enschede, The Netherlands

[3] Engineering Fluid Dynamics Group, Engineering Technology faculty, University of Twente, Enschede, The Netherlands

very specific ratios of flapping frequency and wind speed [6][7][8][9], also known as the optimal Strouhal regime [10]. By measuring (electrical) input power and reaction forces produced by the setup, these hypotheses will be tested. The results can be used to improve future models of the Robird, as current versions have a mechanically fixed phase difference γ and usually fly at a constant flapping frequency.

3) Correlation: By synchronizing the various measurements, they can be correlated. The correlation of force measurements with visualizations of wing flexibility and wake interaction may form a great basis for research on 3D ornithopter aerodynamics and biomimetics.

C. Outline

The remainder of this paper is structured as follows. In Section II, the basic aerodynamics of ornithopter flight are introduced. Section III discusses the actuation and control of the test setup. Next, in Sections IV, V and VI, the methods for, respectively, force measurement, wing reconstruction and wake visualization are presented. The results obtained after processing are shown and discussed in Section VII. Section VIII finishes this paper with conclusions.

II. AERODYNAMICS

Ornithopter flight dynamics have been a topic of research for many years. However, in most cases, strong simplifications have to be made. The most common simplification is that the aerodynamics are considered in 2D instead of 3D. Not only are 3D aerodynamics difficult to model, it is also computationally very expensive to accurately simulate 3D fluid dynamics, especially with a moving object whose flexibility and fluid-structure interaction should also be modelled for accurate results. A mid-way between 2D and 3D is considered for this research: the Robird's wing is divided into strips (see Figure 2), such that 2D aerodynamics can be applied to various sections of the wing.

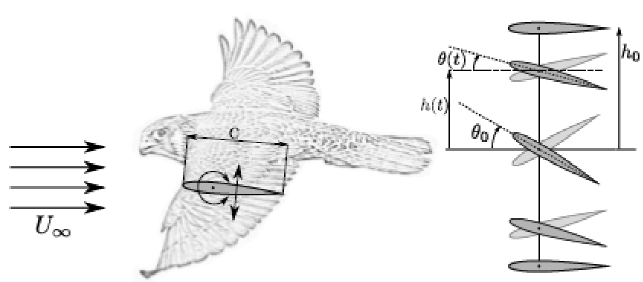

Fig. 2. 2D aerodynamics applied to a strip of the Robird's wing [6].

Figure 2 shows the air velocity U_∞ [m/s] incident to a wing strip of cord length c. The movement of the wing strip with respect to the incoming wind is often (for simplicity and ease of calculation) described as a combination of heave $h(t)$ and pitch $\theta(t)$:

$$h(t) = h_0 \sin(2\pi f t) \quad (1)$$

$$\theta(t) = \theta_0 \sin(2\pi f t + \phi) \quad (2)$$

where h_0 is the heave amplitude, θ_0 is the pitching amplitude and ϕ is the phase shift between the two motions. Often, $\phi = 90°$ is used in experiments and simulations. In the case of the Robird however, both ϕ and the pitching profile in general are unknown and to be determined.

A parameter often used to describe ornithopter flight is the Strouhal number, which relates flapping frequency f, wake width A and flight speed U_∞ as:

$$St = \frac{fA}{U_\infty} \quad (3)$$

Previous research has revealed that for birds, as well as for fish, the Strouhal regime of cruising flight lies approximately between 0.2 and 0.4 [10]. It is therefore believed that this regime is the key to efficient propulsion for the Robird as well. It has to be noted that for his calculations, Taylor chose A to be the wingtip excursion, i.e. twice the amplitude of the tip of the wing. In addition, the Strouhal number can be computed for any other wing strip as:

$$St = \frac{fA}{U_\infty} = \frac{2fh_0}{U_\infty} \quad (4)$$

Finally, we introduce the time-variant effective angle of attack as:

$$\alpha_{\text{eff}}(t) = \arctan\left(\frac{-\dot{h}(t)}{U_\infty}\right) + \theta(t) \quad (5)$$

Previous research showed that both the profile of $\alpha_{\text{eff}}(t)$ as well as its peak value are very important for ornithopter flight [5]. While the profile can take many different forms, it has been revealed that a sinusoidal angle of attack profile resulted in high propulsive efficiency, as well as clean wake interaction [7].

For a more in-depth analysis of the relation between basic strip aerodynamics and the Robird's wing, see Appendix A.

III. ACTUATION

The actuation stage (see Figure 3) resembles exactly one half of a Robird. Each driving rod is actuated by controlling a Maxon EC32 brushless DC motor with an Escon Module 50/5 motor controller. The linkage between motor and driving rod converts one-way rotation into a periodical flapping motion of the wing. For constant motor velocities, the heave profile of the wing is nearly sinusoidal. PID-control schemes, one for the frequency of each driving rod and another for pitch control, are realized in 20-sim and uploaded to a RaMstix FPGA board. Flapping frequency ($f = [0, 6]$ Hz) and relative phase ($\gamma = [0, 15]°$) can then be controlled online by the user via 20-sim 4C [2].

Signals of interest, such as motor position, motor current, frequency and phase difference were logged by the controller at its operating frequency of 500 Hz. Furthermore, the controller was configured to send out a 10 ms pulse once per wing beat, at a user configurable wing angle. This pulse

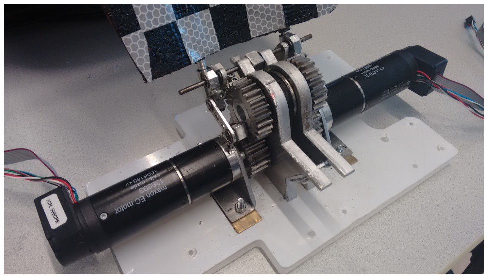

Fig. 3. Actuation mechanism of the setup. Each motor drives one of the wing's driving rods. The phase difference γ between the two rods is limited mechanically at approximately 15°, but can be controlled online. A windshield covers the mechanism during measurements.

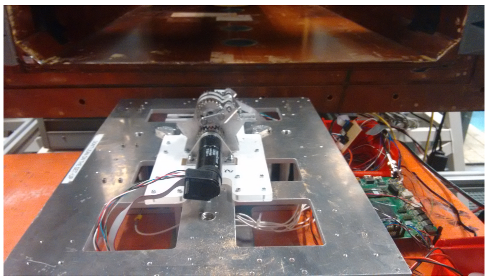

Fig. 4. The actuation mechanism mounted onto the force sensing plate, in front of the wind tunnel. The x-axis of the plate points along the wind's direction and indicates drag forces. The y-axis points to the right and indicates lift forces.

was later used to synchronize measurements and to trigger the PIV system (see Section VI).

IV. FORCE SENSING

A. Force sensing setup

The mechanism is mounted on top of a 6-DOF force sensing plate (see Figure 4), designed and constructed at the University of Twente [11]. The plate houses six wire flexures, each connected to one load cell. Together, they can be used to measure reaction forces (± 50 N range, 9 mN resolution) and torques (± 8 Nm range, 1.5 mNm resolution) in all directions. The raw load cell voltages are first amplified and then received by an xPC target computer running Simulink Real-Time. After subtracting the initial load (due to the weight of the setup), the external force vector is computed and transformed to obtain the force vector acting at the center of the Robird's body. Together with the load cell voltages the controller's trigger pulse is received, allowing for synchronization with current and encoder measurements.

The resulting force vector $F_{\text{meas}} = (F_x, F_y, F_z, T_x, T_y, T_z)$ gives a good indication of the amount of thrust (F_x) and lift (F_y) produced. However, not all of the measured forces are due to aerodynamics: Also measured are inertial forces and stress resultants. Fortunately, these forces will eventually approach a steady-state harmonic behaviour. This means that when averaged over time, the internal forces cancel out and only the mean aerodynamic forces remain.

B. Power and Efficiency

In addition to reaction forces, the efficiency for various control inputs and wind speeds can be evaluated. First, the drag and lift forces can be non-dimensionalized to obtain thrust and lift coefficients $C_T(t)$ and $C_L(t)$ as [8]:

$$C_T(t) := \frac{-F_x(t)}{\frac{1}{2}\rho U_\infty^2 A_{\text{wing}}} \tag{6}$$

$$C_L(t) := \frac{F_y(t)}{\frac{1}{2}\rho U_\infty^2 A_{\text{wing}}} \tag{7}$$

where A_{wing} is the surface area of the wing and ρ is the fluid density of the air. We can determine the electrical input power as the product of the motors' input current and voltage ($P_{\text{in,el}} = I_{\text{m}} \cdot V_{\text{m}}$). However, considering that part of the electrical power is converted to heat and the fact that the actuation setup differs from the actual Robird, it may be more interesting to consider the mechanical power delivered by the motors. Following Folkertsma [12] the (mechanical) energy ΔE supplied to the system during one timestep can be computed by integrating the product of motor torque τ and velocity ω:

$$\Delta E_{\text{in}} = \int_{t_0}^{t_1} \tau(t) \cdot \omega(t) dt \tag{8}$$

Furthermore, since the controller uses a zero-order hold (ZOH) for current control of its motors and we are able to measure angular position $q(t)$ using encoders, we can write:

$$\begin{aligned} \Delta E_{\text{in}} &= \int_{t_0}^{t_1} K_{\text{m}} i(t) \cdot \omega(t) dt \\ &= K_{\text{m}} i(t_0) \int_{t_0}^{t_1} \omega(t) dt \\ &= K_{\text{m}} i(t_0) \cdot (q(t_1) - q(t_0)) \\ P_{\text{in}} &= \frac{\Delta E_{\text{in}}}{(t_1 - t_0)} \end{aligned}$$

where K_{m}=13 mNm/A is the motor's torque constant. The non-dimensionalized input power coefficient is then defined as [8]:

$$C_{\text{in}}(t) := \frac{P_{\text{in}}(t)}{\frac{1}{2}\rho U_\infty^3 A_{\text{wing}}} \tag{9}$$

Finally, the propulsive efficiency η_T over a full wing beat period T is defined as the ratio of the input power coefficient to the thrust coefficient, averaged over time:

$$\eta_T := \frac{1}{T} \int_t^{t+T} \frac{C_T(t)}{C_{in}(t)} \tag{10}$$

Note that, combining (6) and (9), we can also compute the efficiency using the thrust output power P_T:

$$\eta_T = \frac{1}{T} \int_t^{t+T} \frac{-F_x(t) U_\infty}{P_{\text{in}}(t)} dt = \frac{1}{T} \int_t^{t+T} \frac{P_T(t)}{P_{\text{in}}(t)} dt \tag{11}$$

Fig. 5. The imaging setup in the wind tunnel (left) includes an LED stroboscope driven by an Arduino Uno, and two webcams that are read out simultaneously.

V. STEREO VISION

A. Imaging setup

In order to investigate the effects of varying actuation profiles and wind speeds on the flexible behaviour of the wing, a stereo vision set-up is built (see Figure 5). This setup uses a pair of Logitech C922 cameras which are read simultaneously by a laptop running Matlab Simulink. The cameras can only record up to 60 fps, with significant motion blur. Fortunately, since the wing motion is periodic, both disadvantages are overcome by using a stroboscope. The stroboscope consists of LED strips driven by an Arduino Uno [13]. Setting the strobe frequency at 0.9 times the flapping frequency and requiring 100 frames per wing beat (fpb), the minimum on-time T_{strobe} for the stroboscope can be computed as in (12). The amount of motion blur is fully determined by the on-time (1 ms) of the LEDs.

$$T_{\text{strobe}} = \frac{\text{fpb}}{f_{\text{wing}} \cdot 0.9} \tag{12}$$

As shown in Figure 6, the wing is covered in black spray paint and a checkerboard pattern of reflective tape, such that by placing the stroboscope lights close to the camera, maximal contrast between the checkerboard squares can be obtained. This should allow for easy tracking of the keypoints (checkerboard corners) and consequently the 3D reconstruction of the wing's motion. Another checkerboard is fixed to the windshield and defines a static world reference frame.

B. Image processing

The raw video files consist of many black frames, some illuminated frames and some partly illuminated frames. This is depicted schematically in Figure 7: the stroboscope is not synchronised with the cameras' rolling shutters. The black video frames are therefore filtered out and, if the flash was distributed over two consecutive frames, the two are combined. The remaining frames are combined such that the resulting videos capture exactly one wingbeat and their contrast is increased.

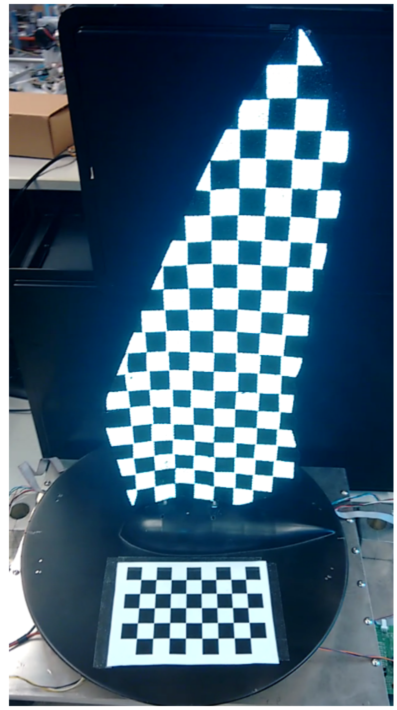

Fig. 6. The wing is covered in black spray paint and a checkerboard pattern made of reflective tape. This increases contrast, and provides many keypoints for tracking. It also allows to apply 2D strip kinematics to the wing. An additional static checkerboard on the windshield defines a world reference frame.

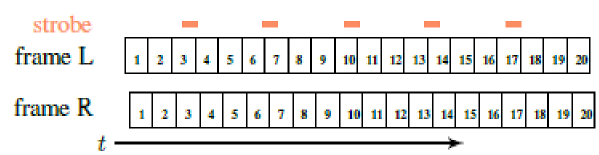

Fig. 7. The stroboscope flashes illuminate only a subsection of the video frames, and might be distributed across two frames. The camera streams are read out simultaneously via USB, but some asynchronicity may be present [3].

C. Tracking and reconstruction

The main reason for the stereo vision measurements is to visualize the flexible behaviour of the wing during flight. This makes tracking challenging; a non-rigid body means that the relative positions of the keypoints change throughout the video in an unpredictable way. Therefore a tracking method based on pose estimation is used.

First, a rigid 3D version of the wing is made using a Structure from Motion approach [14]. This digital template is stored and used as a base wing for tracking. Next, four different modes are defined: flapping, twisting, bending and tilting. A large variety of wing poses can be produced by applying combinations of the four modes to the wing template. Although four modes are not enough to capture the full dynamics of the wing, it has proven to be sufficiently accurate for tracking and it suppresses processing time.

Once a transformation is applied to the template, its corresponding image templates can be produced. Using intrinsic

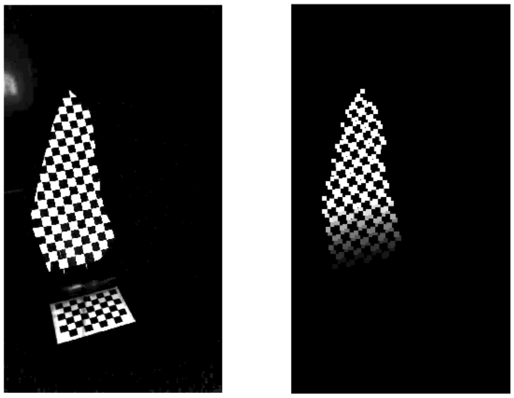

Fig. 8. A real camera frame (left) and a template produced by the pose estimation algorithm for a given set of transformation parameters (right). The product of the two images results in a measure for 'goodness of fit'. The intensity of the template increases along the span of the wing. This forces the tracking algorithm to 'focus' more on the tip of the wing, which is difficult to track due to its flexibility.

and extrinsic camera calibration matrices, the 2D locations of all keypoints are predicted, after which checkerboard corners are projected at these locations. See Figure 8 for an example. The intensity of the projection is scaled, such that the algorithm will focus more on the flexible and unpredictable tip of the wing. A measure for the correctness of the transformation is then obtained by multiplying the image templates with the real video frame. This procedure is repeated a number of times with different mode transformations, after which the best scoring configuration is saved. Additional iterations are needed to more finely tune the transformation parameters. Finally, the best scoring configuration should be a close resemblance of the real image. The exact locations of the keypoints can then be determined more accurately using 2D convolution. The final wing reconstruction for each frame is obtained via triangulation and mesh filtering [15].

For a more in-depth explanation of the tracking and reconstruction process, see Appendix B.

VI. WAKE INTERACTION

Two-dimensional Particle Image Velocimetry (PIV) is used to visualize the effects of the wing on the surrounding air flow. The setup inside the wind tunnel is shown in Figure 9. The laser module produces a horizontal sheet which intersects the wing at a height that is configurable (by moving the entire laser up or down). A particle seeder injects small liquid particles into the flow of air. The high-speed camera, focused at the same height as the laser sheet, then takes two consecutive images, and correlates them to obtain the path and velocity of the particles around the wing. Since the wing is a moving object, the synchronization pulse generated by the controller (see Section III) was used to trigger the camera and laser at desired times, i.e. around the wing's upright position while it was flapping. The PIV measurements were performed at two different heights: around the tip of the wing, and around its mid-section.

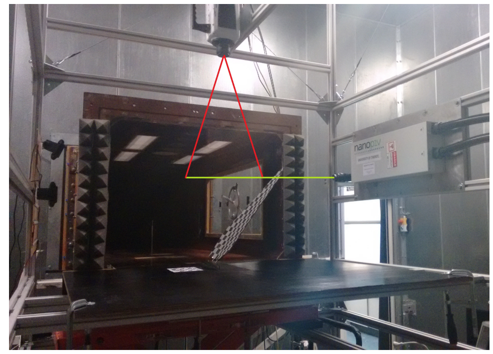

Fig. 9. The setup for Particle Image Velocimetry (PIV) in the wind tunnel. The view of the camera (top) is perpendicular to the sheet produced by the laser (right). In this photo both are focused to capture the flow of particles in a plane surrounding the tip of the wing at the moment it passes its upright position. Later, the laser was lowered and the camera was refocused to capture the flow of particles around the mid-section of the wing.

VII. RESULTS

A. Force measurements

Forces were measured for 55 different combinations of flapping frequency, phase difference and wind speed. A log book of these measurements can be found in Appendix C. Each of the experiments lasted for 20 seconds; the mean force vector F_{meas} was found as the average over the last 50 wing beats within these 20-second time windows. Only the thrust forces (F_x) will be discussed here.

Figure 10 shows curves of the mean thrust force with respect to phase difference γ for various wind speeds. The flapping frequencies were kept constant for each subplot, and the curves have been normalized with respect to the case when no phase difference ($\gamma = 0°$) is introduced. Despite the small set of measurements, one can roughly conclude that at low wind speed, more pitching results in an increase in thrust. In contrast, more pitching leads to a decrease in thrust at higher wind speeds. In the case of $f = 3.65$ Hz and $U_\infty = 14.9$ m/s, drag was measured (here indicated as $F_{x,\text{norm}} = 0$). The hypothesis of high amounts of pitch at high wind speed leading to a reduction of thrust is also confirmed by Figure 13, in which the same negative trend is visualized for various flapping frequencies.

Figure 11 shows curves of the flapping frequency and propulsive efficiency for various flapping frequencies, at a constant wind speed of 14.9 m/s. Added to the top of the graphs are corresponding approximations of the Strouhal number based on wing tip excursion, determined using the stereo vision measurements. We observe strongly varying curves with high peaks at 4.6 Hz and drag being produced at 3.65 Hz. This is in contrast to expectations, as the hypothesis would be that, despite being a highly non-linear system, the thrust increases with increasing flapping frequency. Furthermore, we note that the propulsive efficiency for the case

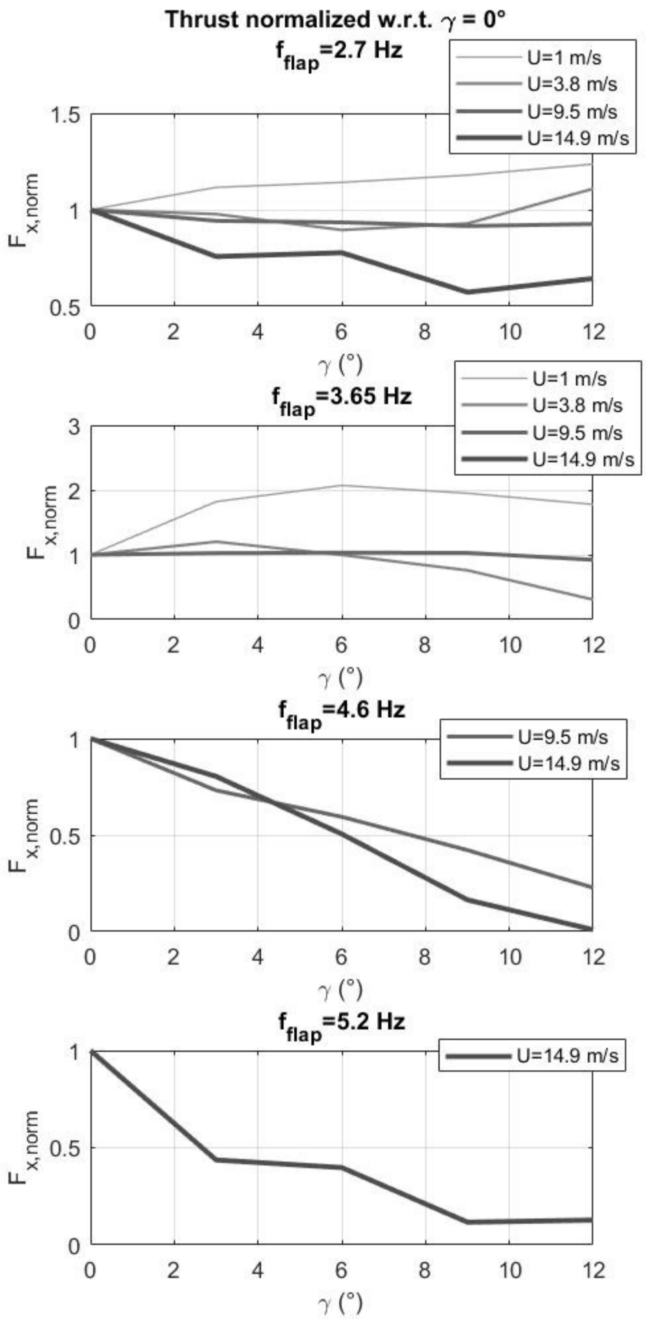

Fig. 10. Measured thrust for two different flapping frequencies, normalized with respect to the case where $\gamma = 0°$. Note that in the case of $f = 3.65$ Hz and $U_\infty = 14.9$ m/s, drag was measured (here indicated as $F_{x,norm} = 0$). The upper plots indicate that increasing γ benefits the production of thrust at low flight velocities while all plots indicate that decreasing γ is preferred at high flight velocities.

of 4.6 Hz is larger than 1, which should be impossible. The cause of this can be found in Figure 12, which visualizes the exchange of power for all 55 experiments. Clearly visible is the increase of input power for increased flapping frequency. The thrust power however, exceeds the input power for some experiments at 4.6 Hz. Apparently the measured forces are incorrect in this case. Although all measurements took place on the same day, recalibrations of the force sensing plate were performed each time the flapping frequency was altered. Another cause may be the large amount of mechanical oscillations experienced by the force plate.

B. Stereo vision measurements

Out of the 55 experiments, the first 40 have been digitally reconstructed using the stereo vision setup and tracking algorithm. For the other (high flapping frequency) measurements, the 1 ms on-time of the LEDs led to significant motion blur, while the illumination of the wing was insufficient at lower on-times. Parameters of interest, including pitch, heave amplitude, effective angle of attack and Strouhal numbers were gathered and added to the overview of experiments which can be found in Appendix C. For conciseness, only the experiments with flapping frequency $f = 2.7$ Hz will be discussed here.

Figure 10 shows the influence of phase difference γ on one of the mid-wing strips. Although differences in the pitching profile can be identified, these are only in the range of several degrees for the larger part of the wing beat. Furthermore we note that in this case, the pitch angle appears to be negative for the larger part of the wing beat. The explanation for this can be seen in Figure 15, where the influence of wind speed U_∞ is shown for the same mid-wing strip. It appears the wind speed is dominating the pitch angle and consequently the effective angle of attack. Less significantly, a higher wind speed appears to slightly reduce the heave amplitude. The explanation for this is in the flexibility of the wing. The wind forces combined with the flapping motion effectively “shape” the wing into a more aerodynamically efficient form. This also causes the wing to gain a pitching motion, even when actuating it at $\gamma = 0$ (see Figure 14).
In literature, the extreme values of the effective angle of attack are often used to characterize ornithopter flight [5][7][8]. As can be seen in Figure 16, the influence of γ on these extrema is very small compared to the effects of the wind speed. This once again proves that the structural design of the wing is very important — arguably even more important than actuation parameters such as phase difference.

C. PIV measurements

Figure 17 shows a single camera image and the resulting vorticity map around the mid-section of the wing for $f = 2$ Hz, $\gamma = 0°$ and $U_\infty \approx 14.9$ m/s. Due to obstruction of the laser sheet by the wing, measurements are only valid on the upper side of the wing and in the wake. A double vorticity street is developed at the trailing edge of the wing (indicated by the blue and yellow layer in the right part of the image). In this case, we observe a street of clockwise

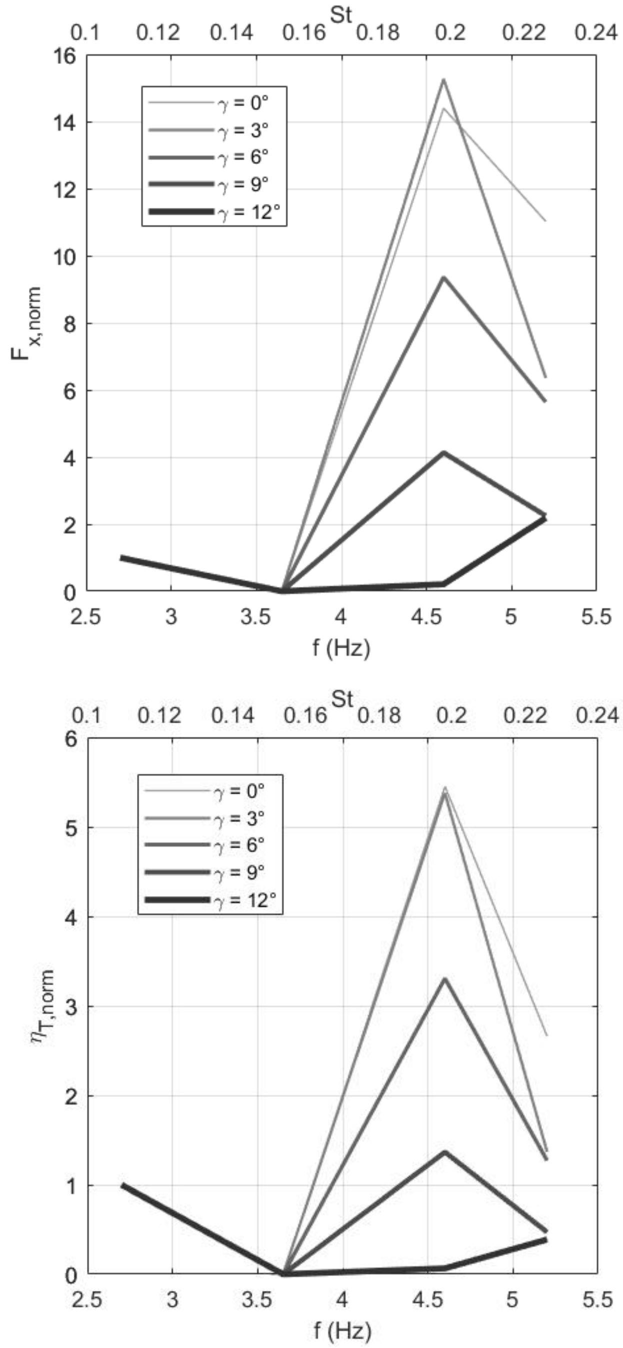

Fig. 11. Measured thrust and propulsive efficiency at constant wind speed $U = 14.9$ m/s, normalized with respect to the case where $\gamma = 0°$. The Strouhal number (upper axis) is based on wing tip excursion and based on stereo vision measurements.

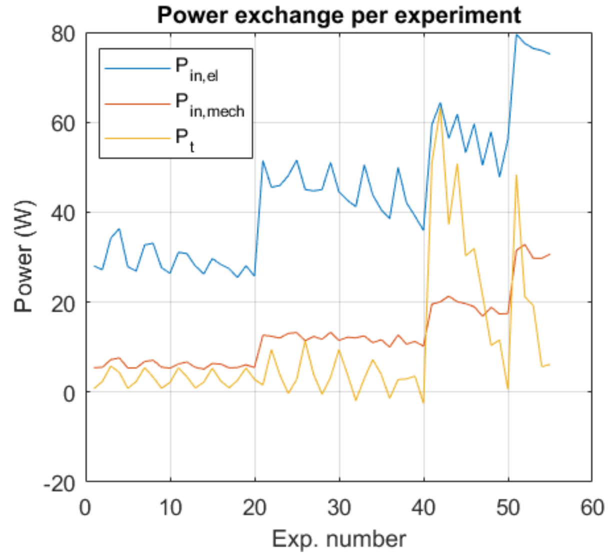

Fig. 12. Input (electrical/mechanical) and output (thrust) power measured for each of the 55 experiments. The force plate was recalibrated each time the flapping frequency was increased, viz. at experiments 21, 41 and 51. For various experiments, P_t exceeds $P_{\text{in,mech}}$, which should not be possible.

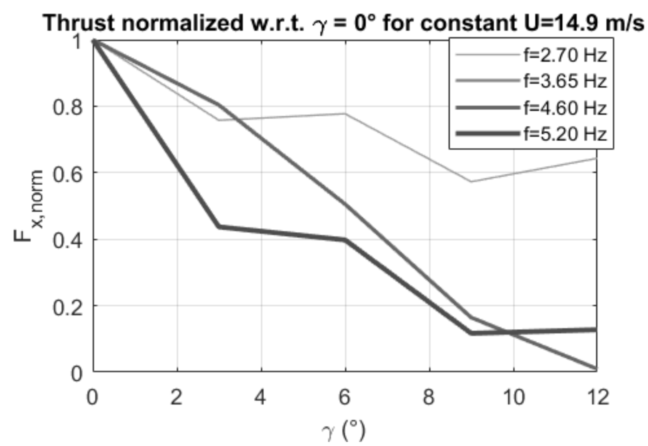

Fig. 13. Measured thrust at constant wind speed $U = 14.9$ m/s, normalized with respect to the case where $\gamma = 0°$. In all cases a negative trend is observed indicating that γ should be small at high flight velocity.

rotation at the top and a street of anti-clockwise rotation at the bottom of the wake. According to wake interaction theory [16], this is an indication of drag. Additional measurements for $\gamma = 10°$ or measurements around the tip of the wing (see Appendix D) did not show notable differences. A logical explanation could be that the ratio of flapping frequency to air speed is too small: the Strouhal number in this case equals 0.097, significantly smaller than the optimum regime of 0.2-0.4 predicted by Taylor [10]. Experience also shows that the Robird is not able to stay airborne at a flapping frequency of 2 Hz. Another explanation could be that the vorticity map differs further down the wake of the wing, i.e. a (reverse) von Kármán street is generated outside of scope of the camera. However, due to lack of mobility of the setup and time, this part of the wake has not been investigated.

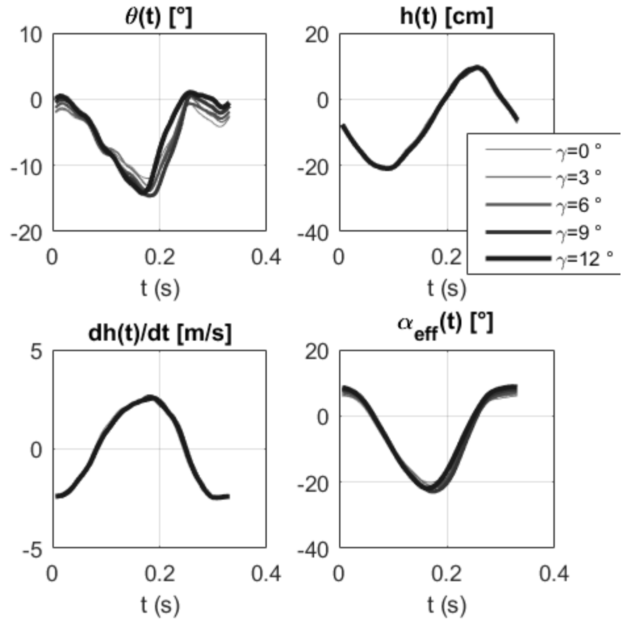

Fig. 14. The influence of phase difference γ: parameters determined by the stereo setup for a mid-wing strip, at $f = 3$ Hz and $U_\infty = 14.9$ m/s. Differences in pitch angle $\theta(t)$ can be observed, especially when the wing is at the end of its upstroke.

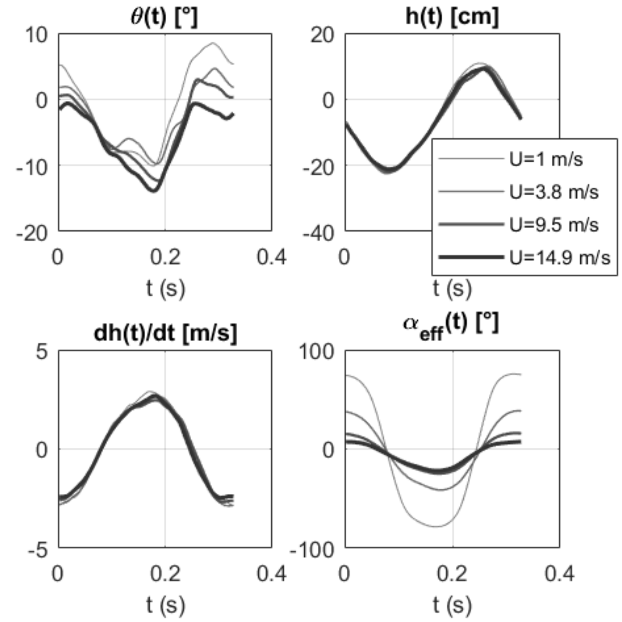

Fig. 15. The influence of wind speed U_∞: parameters determined by the stereo setup for a mid-wing strip, at $f = 3$ Hz and $\gamma = 6°$. Quite clearly the wind speed has a great influence on both the pitching profile as well as the effective angle of attack.

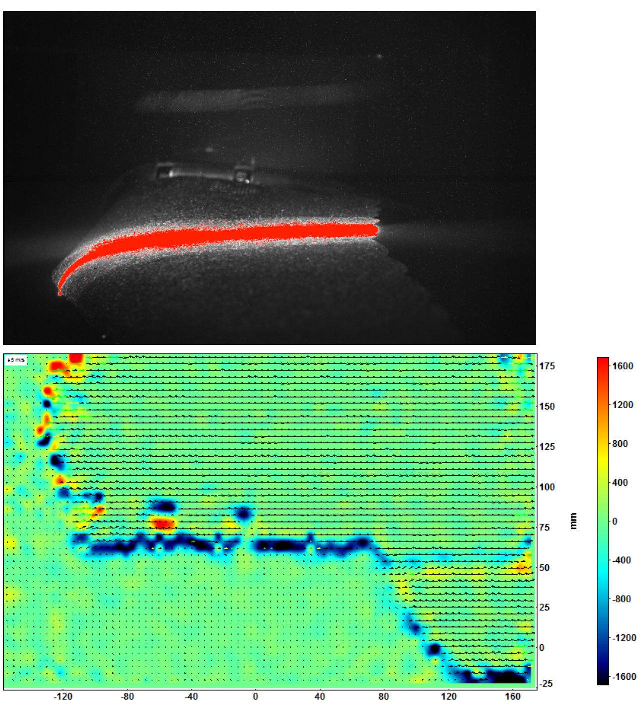

Fig. 17. Top: View of the camera during one of the PIV measurements. The wing is moving downward and has just passed its upright position. The saturated region (red) indicates the height of the laser sheet. Bottom: Z-Vorticity map corresponding to Figure 17, with $f = 2$ Hz, $\gamma = 10°$ and $U_\infty \approx 14.9$ m/s. Blue is clockwise rotation, red is anti-clockwise. We observe a double layer of vorticity generated at the trailing edge of the wing, visible in the right part of the vorticity map.

VIII. CONCLUSION

A large set of experiments has been carried out for different control settings using the flapping wing setup. Force measurements confirm the hypothesis that a variable phase difference between front and leading spar benefits the production of thrust by the robotic bird. In particular, it was shown that pitching angle should decrease as air speed increases. Influence of flapping frequency on production of thrust and propulsive efficiency has been considered as well. However, presumably due to recalibrations of the force sensing plate, no reliable conclusions could be drawn for this case.

"Slow motion" videos produced using the imaging setup were of high quality in terms of motion blur and contrast. The developed computer vision algorithm was able to convert videos into 3D reconstructions despite high wing flexibility. The checkerboard pattern allowed for numerical analysis on individual wing strips as well as the wing as a whole. Measurements revealed that, due to flexibility of the wing, pitching angles and consequently effective angle of attack were dominated by wind speed. The videos and reconstructions can be used for further analysis of flexibility and development of wing models.

Before modifying the pitching mechanism inside the Robird to make the phase difference γ variable, more research on its influence is recommended. The results presented here focus mainly on thrust and propulsive efficiency, while lift forces are just as important for staying airborne. Another topic for future research is the influence of the wing's flexibility. Comparing the current wing model with an older,

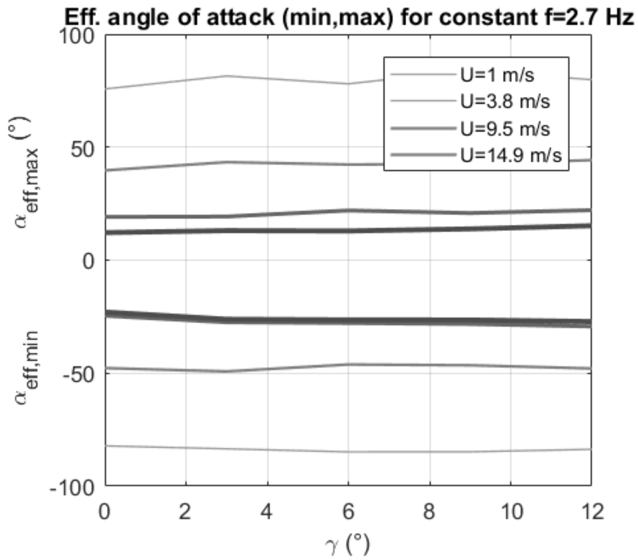

Fig. 16. The influence of γ on the extrema of α_{eff} can hardly be identified compared to the effects of the wind speed.

stiffer version it was noted that the forces measured for the same actuation settings were very different. It is therefore recommended to design multiple wings of different stiffness and compositions, and to compare their performances in the wind tunnel.

Finally, first PIV measurements on the Robird's wing proved the possibility to visualize 2D wake interaction surrounding different wing strips. Further research on different regions around the wing, in particular further down the wake, needs to be performed to properly visualize leading edge vortices and (reverse) von Kármán vortex streets. In addition, multiple 2D measurements at different strips may reveal the flow of LEVs along the span of the wing.

References

[1] C.S.E. Vaseur, S. Stramigioli, G.A. Folkertsma, H.W.M. Hoeijmakers. Robird Wind Tunnel Test Setup Design, November 2014.

[2] C.H. Jongerius, G.A. Folkertsma, J.F. Broenink, A. de Boer. "Real-time" control system for wing twist and flapping frequency, July 2017.

[3] B.A. van der Grinten, G.A. Folkertsma, N. Nijenhuis, S. Stramigioli. Port based Hamiltonian modelling of flapping wing aeroelasticity using vacuum chamber and wind tunnel measurements, September 4, 2015.

[4] S. Heathcote, Z. Wang, I. Gursul. Effect of spanwise flexibility on flapping wing propulsion, Journal of Fluids and Structures 24 (2008) 183-199.

[5] D.A. Read, F.S. Hover, M.S. Triantafyllou. Forces on oscillating foils for propulsion and maneuvering, Journal of Fluids and Structures 17 (2003) 163-183.

[6] J.L. Mulder, H.W.M. Hoeijmakers, H. de Vries, C.H. Venner, R.G.K.M. Aarts. Towards the Understanding of Flapping Wing Propulsion, December 2013.

[7] F.S. Hover, Ø. Haugsdal, M.S. Triantafyllou. Effect of angle of attack profiles in flapping foil propulsion, Journal of Fluids and Structures 19 (2004) 37-47.

[8] J.M. Anderson, K. Streitlien, D.S. Barrett, S. Triantafyllou. Oscillating foils of high propulsive efficiency, J. Fluid Mech. (1998), vol. 360, pp. 41-72.

[9] L. Guglielmini, P. Blondeaux. Propulsive efficiency of oscillating foils, European Journal of Mechanics B/Fluids 23 (2004) 255-278.

[10] G.K. Taylor, R.L. Nudds, A.L.R. Thomas. Flying and swimming animals cruise at a strouhal number tuned for high power efficiency. Nature, 425:707-711, 2003.

[11] J.P. Khatait, D.M. Brouwer, H.M. Soemers, R.M. Aarts, J.L. Herder. Design of an Experimental Set-Up to Study the Behavior of a Flexible Surgical Instrument Inside an Endoscope, Journal of Medical Devices, vol. 7, pp. 1-12, 2013.

[12] G.A. Folkertsma. Energy-based and biomimetic robotics, 2017.

[13] Arduino Uno. Last visited: October 2017. *https://store.arduino.cc/arduino-uno-rev3*

[14] MathWorks. Structure From Motion From Multiple Views. Last visited: September 2017. *https://nl.mathworks.com/help/vision/examples/structure-from-motion-from-multiple-views.html*

[15] G. Peyre. Toolbox Graph, MathWorks File Exchange, 2008. Last visited: October 2017. *http://nl.mathworks.com/matlabcentral/fileexchange/5355-toolbox-graph*

[16] T. von Kármán, J.M. Burgers. General Aerodynamic Theory, Perfect Fluids. 2. J. Springer (Berlin), 1935.

Appendix A: Robird Aerodynamics

In his thesis (Mulder, 2013), Mulder has described the general aerodynamics of (rigid) 2D flapping air foils in a compact but clear way. The analysis will not be repeated here; instead, the most important parameters will be repeated, discussed and related to the Robird.

Parameter	Description & Analysis
$h(t)$	The heaving (up-down) motion of the air-foil in meters. This motion is usually assumed sinusoidal, in the form: $$h(t) = h_0 \sin(\omega t)$$ …where h_0 is the plunging amplitude [m]. For the Robird, h_0 is geometrically variable. Since the heave is introduced by the rotation of the two driving rods, h_0 roughly depends on the distance from this rotation axis as well as the amplitude of the driving mechanism. The reason for assuming a sinusoidal behaviour is because this is both easier in computations as well as in actuation. The Robird's wings are also driven nearly sinusoidally; however, due to the flexibility of the wing and the influence of wind, this may not be the case in reality.
$\theta(t)$	The pitching motion of the air-foil in degrees. This motion is usually assumed sinusoidal as well, in the form: $$\theta(t) = \theta_0 \sin(\omega t + \phi) + \psi$$ …where θ_0 is the pitching amplitude, ϕ is the phase shift between the heaving and pitching motion and ψ is the pitch bias. Similar to the heave amplitude, θ_0 is geometrically variable for the Robird. The pitch in this case is the result of a phase difference γ between the motion of the two rods. For the current version of the Robird, γ is held constant at 7° simply because the flight performance is satisfactory. As the 'front' rod leads the 'back' rod, a difference in heave is introduced between the front and the rear side of the wing. This difference in heave is small at the base of the wing, but increases when moving towards the tip. The stiffness of the wing and the flexibility of the rods counteract this twisting effect, making the pitch amplitude very difficult to estimate or control. Due to the high flexibility near the wing tip relatively large pitching amplitudes are expected in this region. The influence of the phase shift ϕ is still very much unknown. In most analyses and research, this parameter is assumed or set to 90°, i.e. the pitch leading the plunge. Again, this simplifies computations as well as actuation. Read (Read, 2003) experimented with this value and identified a regime of $\phi = [90{,}100]$ in which optimal thrust and efficiency were generated for an oscillating foil in water. In contrast, Anderson (Anderson, 1998) identified a phase shift of $\phi = 75$ to be optimal for both production of thrust and efficiency. He described the phase angle as being "the critical parameter affecting the interaction of leading-edge and trailing-edge vorticity, as well as the efficiency of propulsion". For the Robird, since the pitching and the plunging motion are both caused by the same near-sinusoidal driving mechanism, ϕ should in theory be approximately equal to

	90° (assuming the front rod leads the back rod). It is however expected that this parameter is again heavily influenced by wing flexibility and wind forces. The pitch bias ψ is in general viewed as the key parameter defining the ratio of produced thrust and lift forces. This has been confirmed by Read (Read, 2003). Assuming a constant air velocity and direction, this parameter can be most easily controlled during flight by actively pitching the entire Robird, for example by steering the Robird's tail flaps. The pitch bias is therefore held at 0 throughout this research.
k	The reduced frequency, defined as: $$k = \frac{2\pi fc}{U_\infty} = \frac{\omega c}{U_\infty}$$ …where U_∞ is the free-stream velocity or flight velocity in meters per second and c is the cord length in meters. The reduced frequency is a measure for the flapping frequency relative to the flight speed. Since c varies across the Robird's wing, k does as well.
St	The Strouhal number, defined as: $$St = \frac{Af}{U_\infty} \approx \frac{2h_0\omega}{2\pi U_\infty} = \frac{kh_0}{\pi c}$$ …where it is usually assumed that the characteristic width A of the created jet flow is equal to twice the heave amplitude of the tip of the wing. Accurately predicting or determining the real value of A is difficult. The Strouhal number has been a key parameter for the study of efficiency and thrust generation in a large number of studies, including studies of flying and swimming animals. A summarizing study by Taylor (Taylor, 2003) shows that the Strouhal number for many animals (when cruising) lies between 0.2 and 0.4. It is therefore assumed that this is a region of optimal efficiency which should also be of great importance for the Robird.
$\alpha_{eff}(t)$	The effective angle of attack, defined as: $$\alpha_{eff}(t) = \arctan\left(\frac{-\dot{h}(t)}{U_\infty}\right) + \theta(t) \approx -\arctan(\pi St cos(\omega t)) + \theta(t)$$ …where the second version is again under the assumption that the heaving motion is sinusoidal. $\alpha_{eff}(t)$ is perhaps the most influential parameter of flapping wing flight as has been shown by previous research. Because of the mathematical composition of $\alpha_{eff}(t)$ and its dependence on both tuneable and environmental parameters, its periodical profile can vary a lot. To illustrate this, consider the angle of attack profiles computed by Read for various values of St, show in Figure 1.

<table>
<tr>
<td></td>
<td>
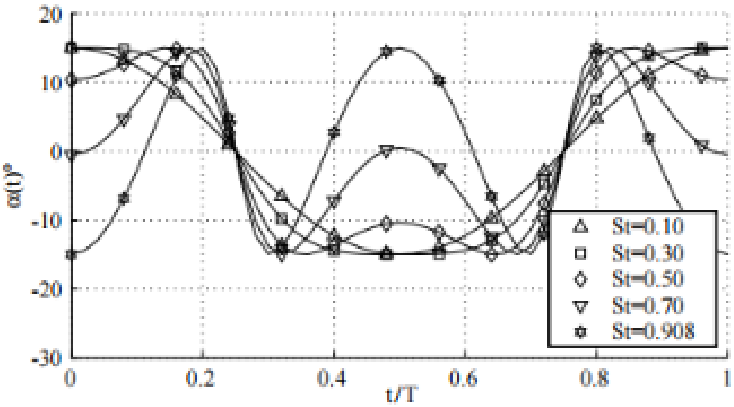

Figure 1: Angle of attack profile of an oscillating foil showing the result of increasing Strouhal number for $\psi = 90°$, $\alpha_{max} = 15°$ (Read, 2003).

As the Strouhal number increases, the angle of attack profile converges from a near-sinusoidal shape towards a square wave, and finally more odd harmonics with multiple minima and maxima per wing beat. Hover researched the effect of this degraded profile through a series of measurements (Hover, 2004). His observations showed that the angle of attack profile was strongly related to the propulsive efficiency of a flapping foil in water. This was best seen through visualizations of the vorticial pattern in the foil wake; a sinusoidal angle of attack profile resulted in two clean vortices per wing beat while a degraded angle of attack profile resulted in additional, drag-producing vortices. Hover also compared different angle of attack profiles by adjusting the heave motion profile. Both a sawtooth and a square wave angle of attack profile proved to be less efficient than (near-)sinusoidal profiles, though under the right circumstances the sawtooth profile was able to create a strong increase in thrust.
</td>
</tr>
<tr>
<td>C_T, C_L</td>
<td>
When studying the aerodynamical forces and efficiency of a flapping wing, it is important to assign clear definitions to them. These forces are in literature often described by non-dimensional thrust and lift coefficients $C_T(t)$ and $C_L(t)$, or $\overline{C_T}$ and $\overline{C_L}$ when averaged over one complete flapping period $T = 1/f$:

$$C_T(t) \coloneqq \frac{-Drag(t)}{\frac{1}{2}\rho U_\infty^2 A_{wing}}$$

$$C_L(t) \coloneqq \frac{Lift(t)}{\frac{1}{2}\rho U_\infty^2 A_{wing}}$$

…with ρ the fluid density [kg/m^3] and A_{wing} the area of one of the sides of the wing.

For a 2D case, both the drag and lift forces are usually determined at the origin of the pitching axis. For the Robird, eventually, the reaction forces are most interesting when transposed to the body of the bird.
</td>
</tr>
<tr>
<td>C_P, μ</td>
<td>
Similarly, the mechanical input power can be made non-dimensional using the input power coefficient $C_P(t)$:

$$C_P(t) \coloneqq \frac{P(t)}{\frac{1}{2}\rho U_\infty^3 A_{wing}}$$

By relating the thrust and lift coefficients to the input power, we can finally obtain the efficiency η for both thrust and lift production:
</td>
</tr>
</table>

	$$\eta_T = \frac{\overline{C_T}}{\overline{C_P}}$$ $$\eta_L = \frac{\overline{C_L}}{\overline{C_P}}$$ The actuation and propulsion of the Robird are dominated by the motors driving each of its wings. The input power can thus easily be determined by monitoring the power required by its motors.

Previous Measurements and Simulations

In 2013, Mulder performed numerical simulations on a model of the Robird's wing using a 2D complex fluid dynamics solver at three different sections of the wing. He found that the root of the wing mainly provides lift, while the tip of the wing mainly provides thrust. The mid-wing section provided a balance of the two. The efficiency peaked for Strouhal numbers between 0.1 and 0.3, all at a maximum effective angle of attack of 11 degrees, which corresponded with the angle of attack of static stall. Furthermore, he noted that large thrust forces were obtained for smaller pitch amplitudes at small Strouhal numbers, and for larger pitch amplitudes at large Strouhal numbers. This indicates that it may be beneficial to be able to adapt the pitching amplitude during flight. Finally, he predicted the resulting jet profiles in the wake of the wing using simulations and measured them in a wind tunnel, finding acceptable agreement between the two.

Appendix B: Tracking and Reconstruction

A new tracking algorithm was developed in Matlab, in order to be able to process both the previous video measurements performed by van der Grinten (van der Grinten, 2015) and new video measurements. Inspiration for the tracking algorithm was based on reports by him and van de Ridder (van de Ridder, 2016). Furthermore, the following points have been taken into account for the algorithm development:

- Processing time: Optimization algorithms and image processing are a computationally expensive combination. On the other hand, many videos will have to be processed. This means that the tracking algorithm should not only be powerful and precise, but also fast and efficient. Furthermore the amount of manual workload should be minimized in order to enable batch processing.
- Use of pre-knowledge: The video measurements are accompanied by a log book showing the exact control parameters of the measurement setup for every video. This knowledge can be used by the tracking algorithm for faster and more accurate tracking. The position of each marker on the wing (assuming a rigid wing) is also useful pre-knowledge.
- Focus on the tip: Due to the low stiffness near the tip of the wing, this part is very flexible, unpredictable and therefore hard to track. Extra measures need to be taken to also correctly track this part of the wing.

Video pre-processing

One of the things that can hardly be automated and thus still have to be performed by hand is the pre-processing of video measurements. Van der Grinten developed Matlab code to convert the raw videos and sort them such that only the frames that were lighted by the stroboscope remained. However, these videos (2 per camera) form only just over half of a wing beat. For further analysis the videos have to be merged in such a way that the videos cover exactly one wing beat, while both the left and right camera frames remain synchronized. A simple Matlab tool (Figure 2) has been made for this, which allows for quick previewing and exporting of full wing beat videos for the left and right camera simultaneously.

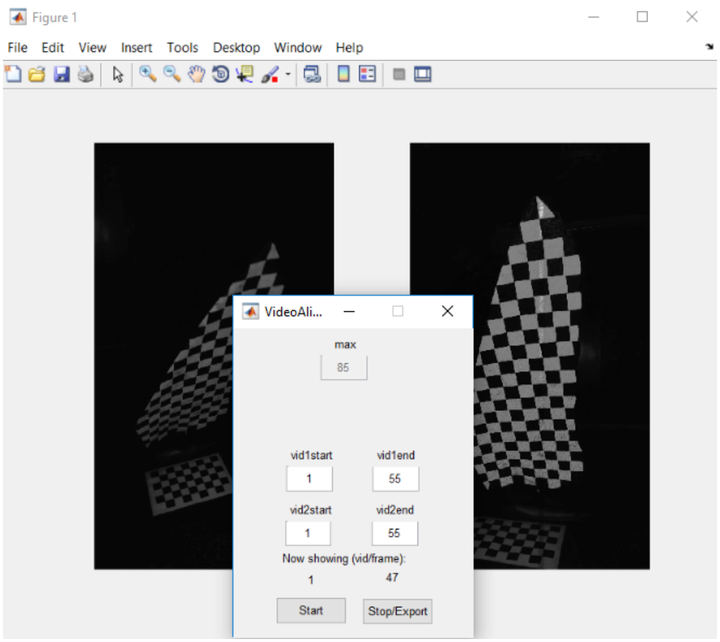

Figure 2: Snapshot of the video alignment tool.

Reference frames

The base of the designed tracking algorithm operates in the wing reference frame O_{wing}, see Figure 3. This shows the bottom side of the old wing used by van der Grinten during measurements, covered with 49 "checkerboard corners". Indicated is the wing reference frame, with its origin at the pivot point of the wing. This point is the origin for both the heaving and the pitching modes of the wing and thus of major importance for automated tracking. Since this point does not move, the relative position and orientation with respect to the world reference frame (defined by the checkerboard on the windshield) is constant and known. By detecting the checkerboard in the video frames, the orientation and position of the cameras in the world reference frame can be determined as well. In other words, we have approximated the transformation matrices H between the cameras' reference frames O_{camL} and O_{camR}, the world reference frame O_{world} and the wing reference frame O_{wing}. See Figure 4 for a graphical representation of this.

Throughout the processing of the videos these transformation matrices were assumed to be constant, i.e. the cameras did not move with respect to the wing setup. This allows to estimate the matrices once, such that they can be used for all videos that belong to the same measurement sequence. Estimating the origin of the wing reference frame for every individual video by incorporating it in a pose estimation algorithm, as proposed by van de Ridder, scales up the computational load significantly and was not expected to improve tracking accuracy significantly.

Figure 3: Left: Wing reference frame O_{wing} with origin at pivot point, indicated on an <u>older</u> version of the wing. Right: Cropped video frame showing the pivot point.

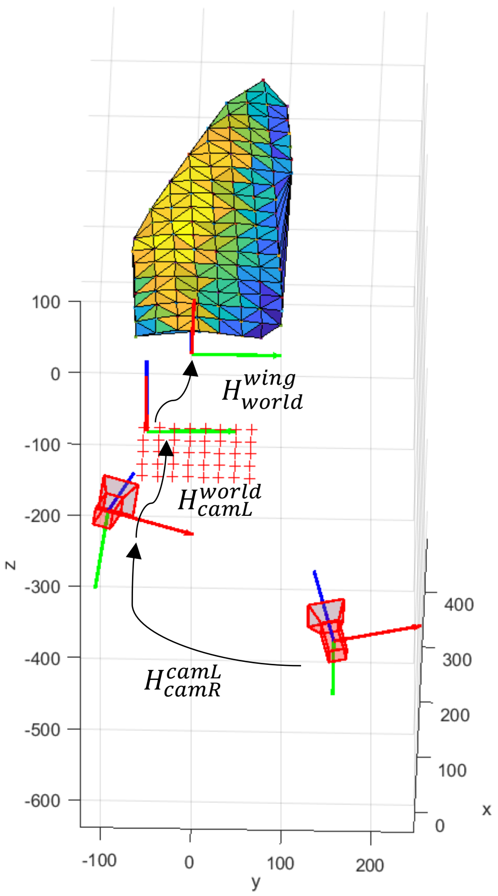

Figure 4: Reference frames and their transformation matrices. H_{camR}^{camL} is known from camera calibration, H_{camL}^{world} is determined by detecting the windshield's checkerboard in the video frames, and H_{world}^{wing} is static and known.

Pose estimation

The core of the tracking algorithm is an optimization routine based on pose estimations, similar to that of van de Ridder. A wing template is constructed using a Structure from Motion (SfM) approach; the wing is photographed from various angles, its checkerboard corners are identified in each image and triangulated (see Figure 5). The rigid wing template contains the 3D coordinates and marker rotations of every marker with respect to the wing reference frame.

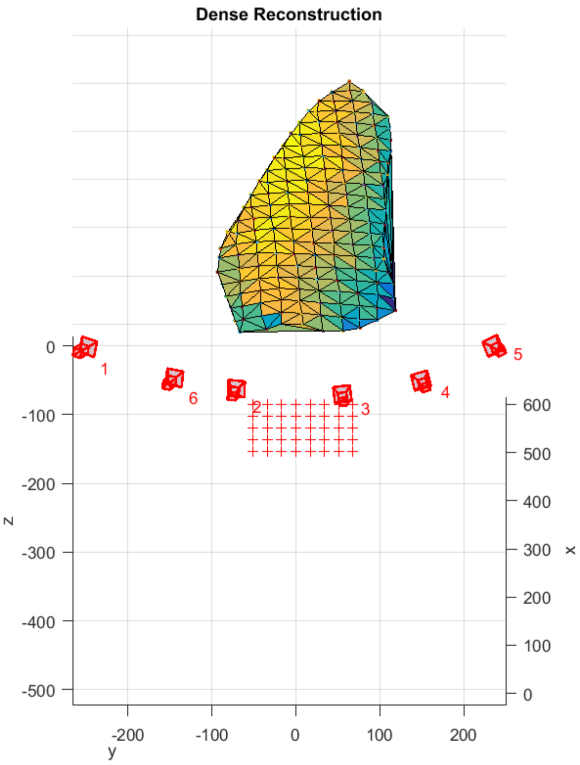

Figure 5: 3D reconstruction of the rigid static wing using a Structure from Motion (SfM) approach. The red grid indicates the windshield checkerboard.

Next, four transformation modes/parameters have been defined to model the pose of the wing throughout the video (Demonstrations of the four transformation modes are shown in Figure 7.):

- Heaving/flapping; heave introduced by the up-down motion of the driving rods. This transformation is performed by simply rotating the 3D marker coordinates by an angle ϕ around the y-axis of O_{wing}.

- Bending; additional heave dependent on the distance r from the pivot point as a result of inertia and wind forces. In order to suppress processing time, a single bending mode is defined. The amplitude of the additional heave is linearly dependent on r and given by:

$$\beta_0(r) = rC_b$$

…where C_b is a constant tuned and set to $4 \cdot 10^{-4}$.

- Tilting: tilting introduced by the play in the connections between the driving rods and the wing itself. This transformation is performed by simply rotating the 3D marker coordinates by an angle χ around the z-axis of O_{wing}.

- Twisting; the twisting mode of the wing introduced by the phase difference between the two rods, in its turn leading to a heave difference between the two rods. This is illustrated in Figure 6, showing the maximum height difference $\Delta h_0(r)$ between the two rods, where $\Delta h_0(r)$ is given by:

$$\Delta h_0(r) = 2rC_t sin\left(\frac{\gamma}{2}\right)$$

…with γ the phase difference between the rods, r is the distance from the pivot point and C_t is a constant representing the torsional compliance of the wing. C_t was tuned and set to 0.08. The pitching amplitude $\theta_0(r)$ around the x-axis of O_{wing}, induced by the phase difference γ can then be determined as:

$$\theta_0(r) = \arctan\left(\frac{\Delta h_0(r)}{b}\right) = \arctan\left(\frac{2C_r r}{b} sin\left(\frac{\gamma}{2}\right)\right)$$

…where $b = 0.062$ $[m]$ is the distance between the pivot points of the two rods.

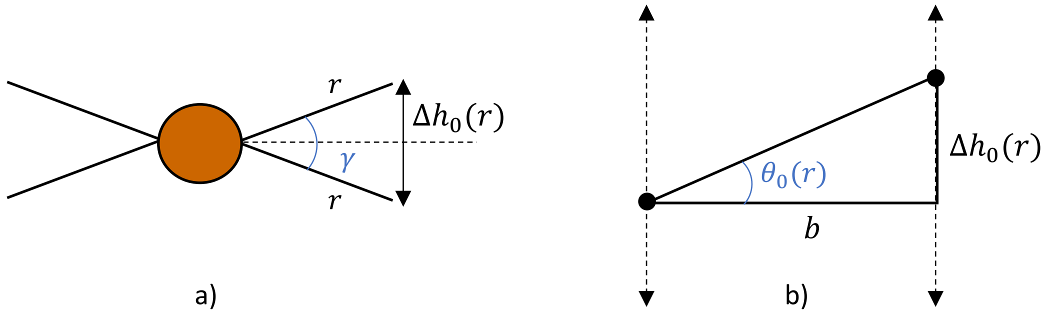

Figure 6: a) Front/back view and b) side view of the Robird's driving rods, used to derive the pitch amplitude $\theta_0(r)$.

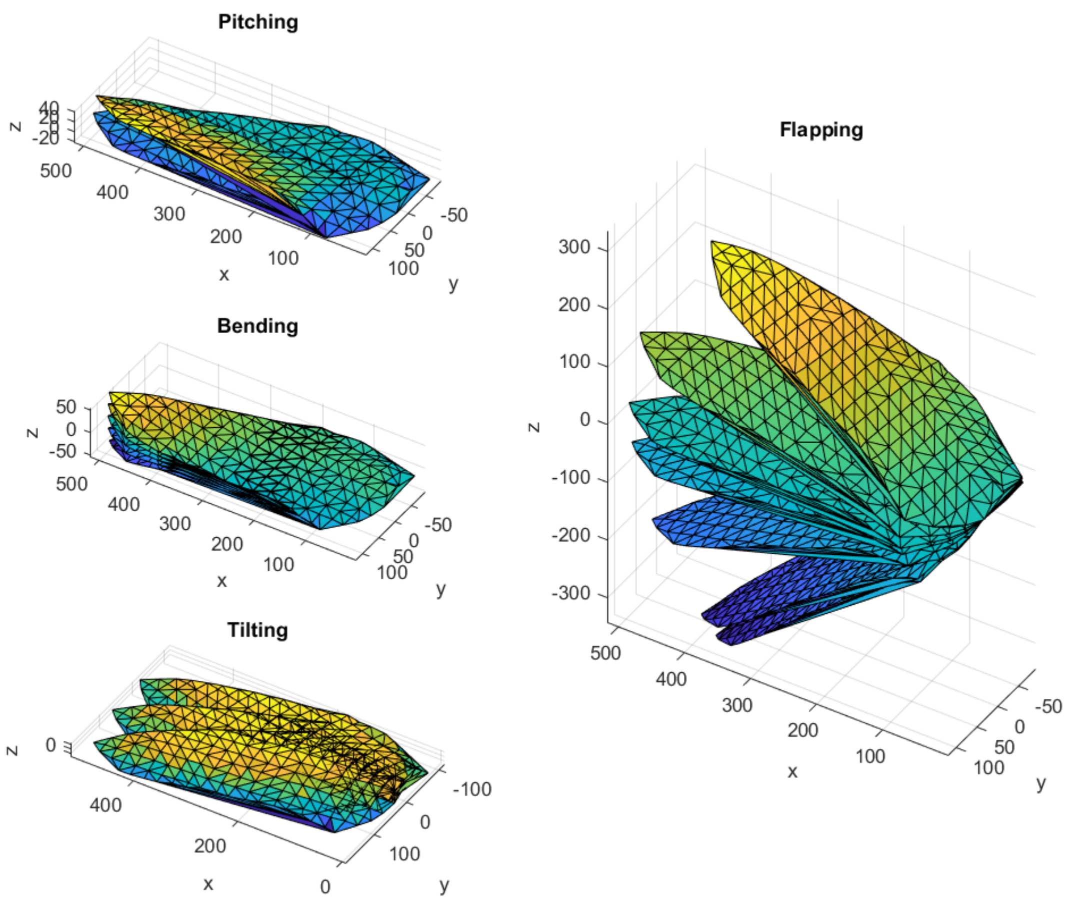

Figure 7: Demonstration of the four modes used to estimate the pose of the wing.

Pose optimization and convergence

After using the four pose parameters to transform the wing in its own 3D reference frame, the camera calibration parameters[1] and transformation matrices can be used to transform these coordinates $\boldsymbol{x}_{wing}$ into 2D image coordinates $\boldsymbol{x}_{cam}$. This allows us to apply a transformation to the wing template, and then to 'project' each marker in the camera frames of both images. Using the orientation of each marker (pre-knowledge) and the 3D distance between the marker and the camera, we can predict how each marker should look like from each camera's view in terms of size and orientation. An example of such a wing projection is shown in Figure 8. Note the difference in intensity between the markers: Each individual marker is first normalized such that the sum of its pixel intensities equals 300 (using signed int8 greyscale video). Next, a weight is applied by multiplying each marker with the distance r between the marker and the origin of the wing frame. This increases the intensity of markers near the edge/tip of the wing.

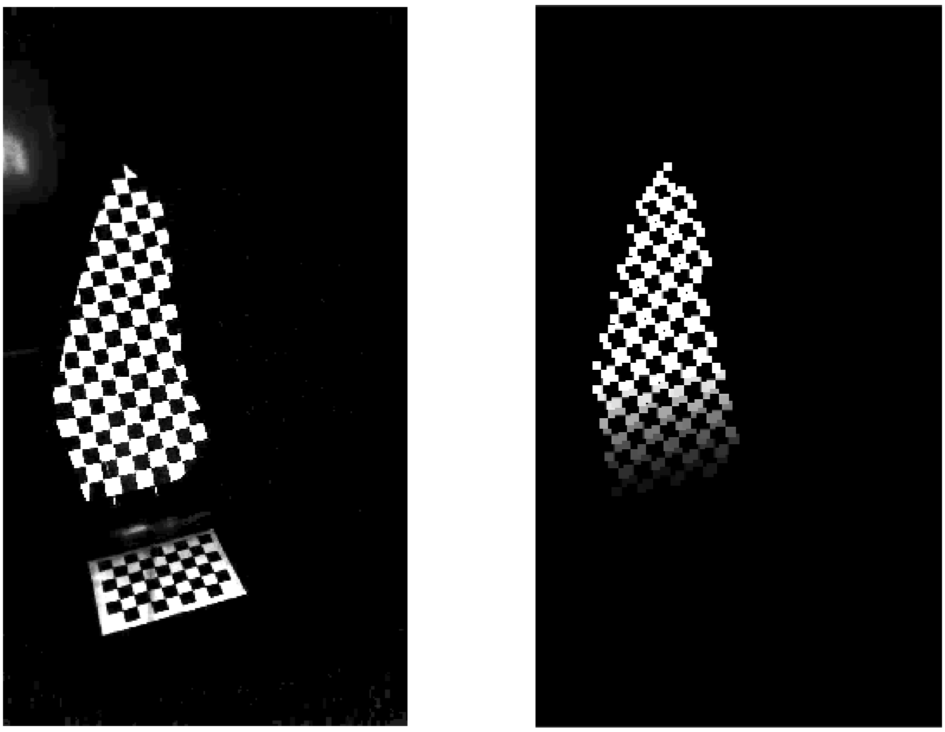

Figure 8: A real camera frame (left) and a template produced by the pose estimation algorithm for a given set of transformation parameters (right). The product of the two images results in a measure for 'goodness of fit'.

The optimization routine is performed using these artificial projections, the real camera images and a grid of transformation parameters. Given a predicted set of normalized parameters $\left[\bar{\theta}(t), \bar{\phi}(t), \bar{\beta}(t), \bar{\chi}(t)\right]$, each in the range of $[-1,1]$, such that

$$\theta(t) = \theta_0(r)\bar{\theta}(t)$$

[1] Both cameras have been calibrated simultaneously using Matlab's Stereo Camera Calibration Tool and a checkerboard with squares of 25.3mm width/height. Calibration results can be found in the folder *'../camera_calibrations/calib_21-8_25.3mm'*.

$$\phi(t) = \phi_0\bar{\phi}(t)$$

$$\beta(t) = \beta_0(r)\bar{\beta}(t)$$

$$\chi(t) = \chi_0\bar{\chi}(t)$$

We can define a grid around these predicted, normalized parameters:

$$\bar{\theta}_{grid} = [\bar{\theta} - \delta_\theta, \bar{\theta} + \delta_\theta]$$

$$\bar{\phi}_{grid} = [\bar{\phi} - \delta_\phi, \bar{\phi} + \delta_\phi]$$

$$\bar{\beta}_{grid} = [\bar{\beta} - \delta_\beta, \bar{\beta} + \delta_\beta]$$

$$\bar{\chi}_{grid} = [\bar{\chi} - \delta_\chi, \bar{\chi} + \delta_\chi]$$

…with δ_x the grid step size for each parameter. Taking a default resolution of $R = 5$ grid values per parameter this means a total of $N = R^4 = 625$ pose estimations can be made per iteration. For each pose estimation, the artificial projections are made. A score for each pose is obtained by multiplying the artificial projection with the real image and taking the sum of all pixels. The combination of parameters resulting in the best score is saved. Running multiple optimization routines with different grid settings in series allows for higher accuracy, but obviously requires more processing time.

Based on pre-knowledge and observation both the heave profile and the bending profile are approximately known and therefore rather easy to predict, i.e:

$$\phi(t) = \phi_0\bar{\phi}(t) \approx \phi_0 \sin(\omega t)$$

$$\beta(t) = \beta_0\bar{\beta}(t) \approx \beta_0 \sin^8(\omega t)$$

However, although the videos cover exactly one full wing beat, they can start anywhere during the stroke, which introduces a random and unknown phase difference. This phase difference is determined by starting with a partial optimization routine for only $\bar{\phi}(t)$ with $\delta_\phi = 0.5$. The result is a very low-resolution estimate of the heave profile, but by fitting a sine wave to this time series a decent initial estimate of the heave profile is obtained. Based on this, an initial estimate for the bending mode is made as well. See Figure 9 for an example. For the available video measurements, this is followed by several more optimization iterations. An example of final estimates of the modes is shown in Figure 10.

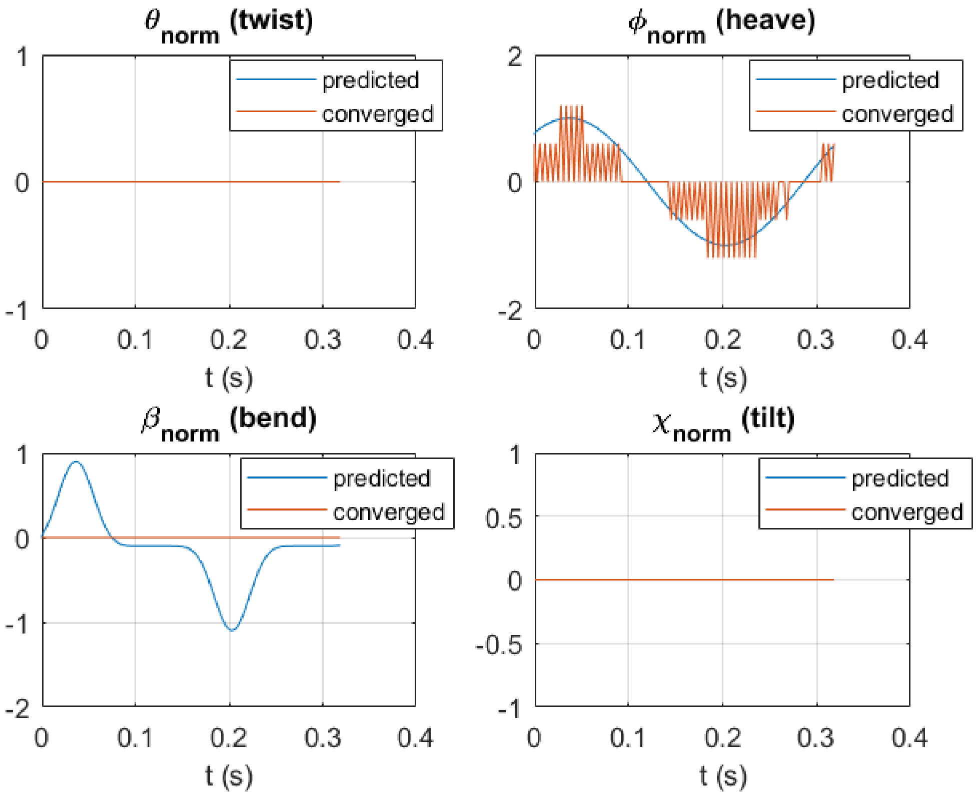

Figure 9: Results of the first iteration: heave is estimated for every 2nd video frame, while pitching, bending and tilting modes are disabled. Sine-fitting the heave estimates gives a quick, easy and decent estimate of the heave profile for further optimization routines. The bending profile is also predicted as bending mostly occurs at the end of upstroke and downstroke.

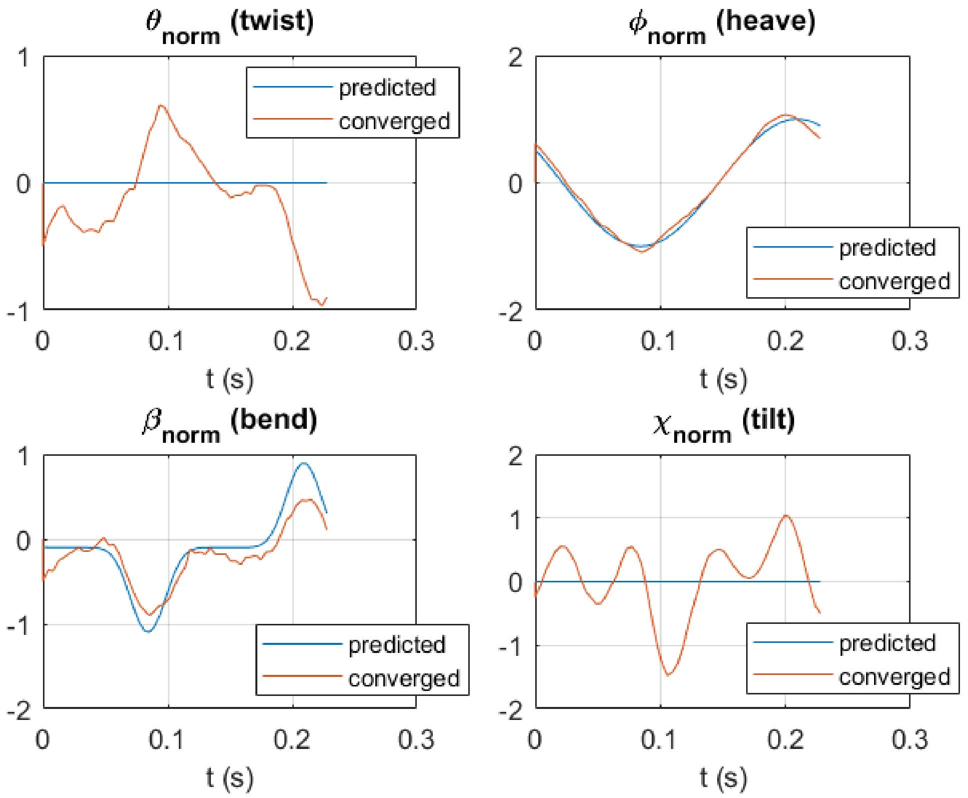

Figure 10: Results after the final iteration. Heave and bending profile were quite predictable, in contrast with the twisting and tilting modes.

Finally, during the last optimization routine, the locations of the marker projections should be accurate enough to be able to use 2D convolution. Each projected marker is convoluted with a small region around the estimated location of the 2D image and the coordinates of highest correlation are returned. Via triangulation of the image coordinates the corresponding 3D coordinates are obtained, see . Delaunay triangulation is applied to create a mesh of the wing for each video frame. Due to errors made by the tracking algorithm in the 2D image frame, some “noise” is still visible in the form of spikes on the mesh surface. Fortunately, we know that the wing surface remains a smooth surface at all times. Therefore, 3D mesh filtering is applied (Peyre, 2008). This basically removes any spikes occurring on the 3D wing surface. An overview of the full tracking process is shown in Figure 12.

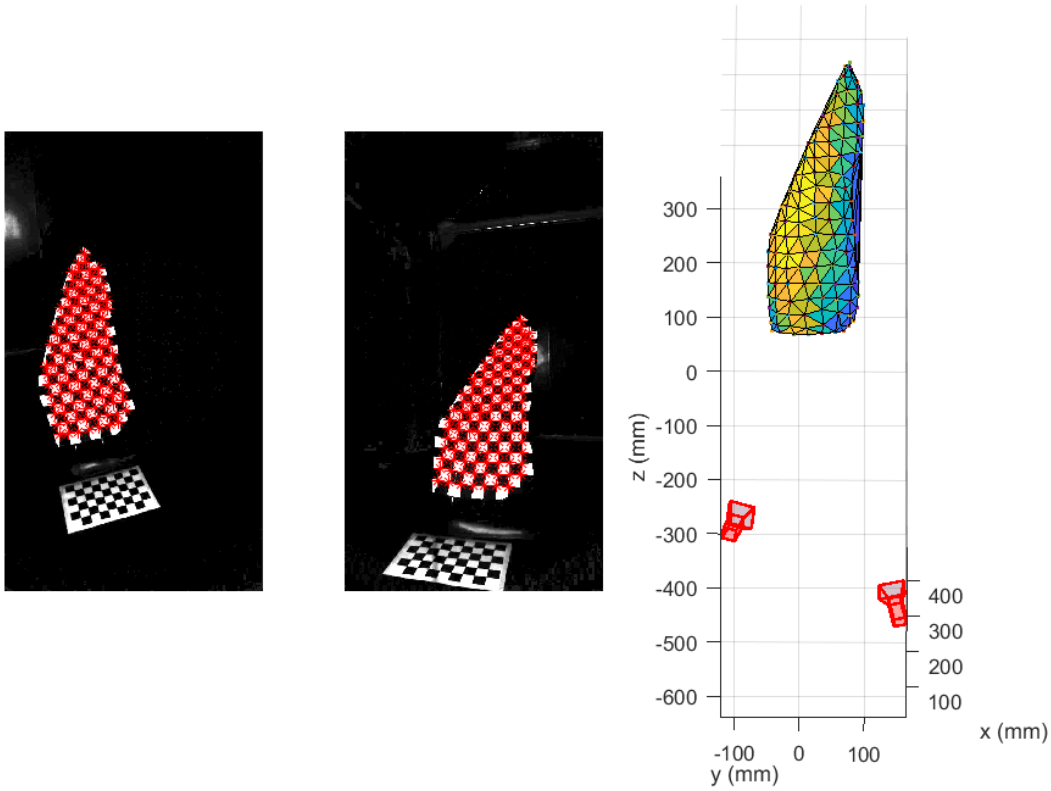

Figure 11: Given an accurate wing configuration, all key points can detected by 2D convolution in the image frames (left). Next, the 2D coordinates are triangulated and mesh surface filtered to obtain the final 3D reconstruction (right).

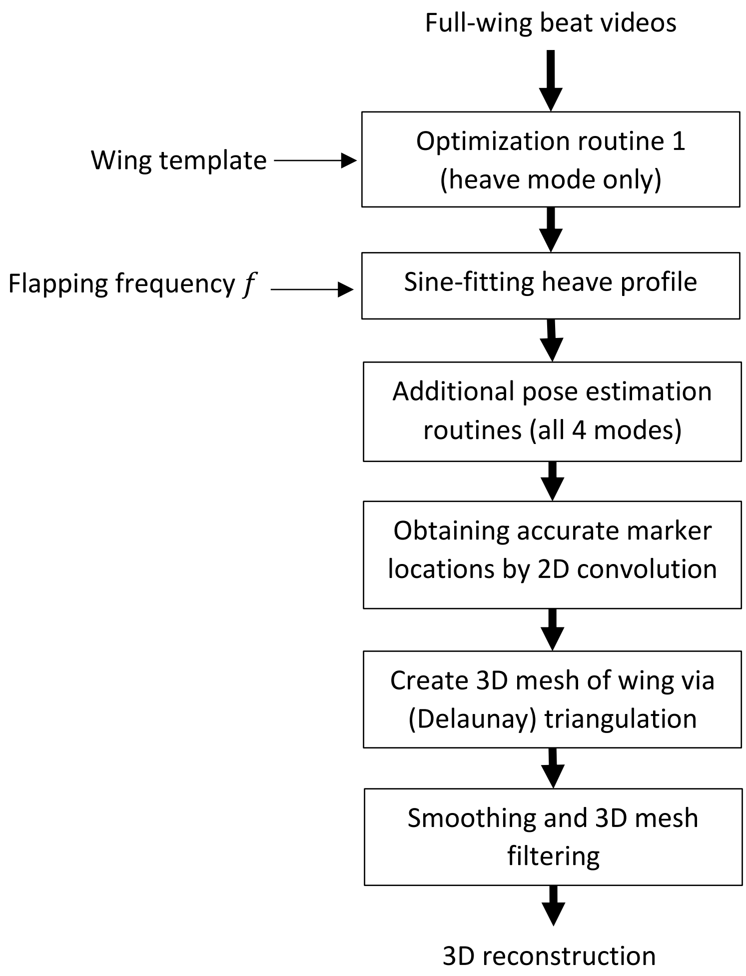

Figure 12: Overview of the tracking process for a full wing beat.

Appendix C: Overview of wind tunnel experiments

Notes:

- An extended version is available as 'WindTunnelLogbook.xls'.

- Stereo vision measurements were only performed for experiments 1-40.

- The wind speed U_∞ is assumed 1 m/s when the wind tunnel was off, in order to account for air flow due to flapping and to avoid zero division when calculating Strouhal number and effective angle of attack.

- The actual flapping frequency differs from the set flapping frequency because the relation between encoder counts and flapping frequency was not as expected. The actual flapping frequency is computed by counting the amount of wing beat triggers over the full experiment and dividing by time (see also Figure X). This also means that the actual phase difference may differ from the set phase difference, but this could not be measured.

Day	Exp.	f (Hz)	γ (deg)	U_∞ (m/s)	Actual f (Hz)	Mean thrust (N)	St (tip)	h_0 (tip) (mm)	$\alpha_{eff,max}$ (mid) (deg)	$\alpha_{eff,min}$ (mid) (deg)
Aug 18/08										
	1	3	0	1,0	2,70	0,754	1,829	338,6	75,8	-82,2
	2	3	0	3,8	2,70	0,628	0,459	323,2	39,7	-47,8
	3	3	0	9,5	2,75	0,609	0,179	309,5	19,2	-24,6
	4	3	0	14,9	2,70	0,295	0,109	302,0	12,2	-23,0
	5	3	3	1,0	2,70	0,842	1,823	337,7	81,5	-83,5
	6	3	3	3,8	2,75	0,614	0,477	329,7	43,4	-49,2
	7	3	3	9,5	2,70	0,574	0,176	309,4	19,3	-27,5
	8	3	3	14,9	2,70	0,223	0,110	302,2	13,1	-26,1
	9	3	6	1,0	2,70	0,861	1,847	342,1	78,0	-84,8
	10	3	6	3,8	2,70	0,562	0,454	319,8	42,3	-46,2
	11	3	6	9,5	2,70	0,570	0,174	306,8	22,0	-27,8
	12	3	6	14,9	2,70	0,229	0,109	299,6	12,9	-26,4
	13	3	9	1,0	2,70	0,889	1,798	333,0	83,9	-84,8
	14	3	9	3,8	2,75	0,584	0,473	326,7	42,5	-46,5
	15	3	9	9,5	2,75	0,558	0,176	303,6	20,8	-28,3
	16	3	9	14,9	2,70	0,169	0,108	298,8	13,8	-26,5
	17	3	12	1,0	2,70	0,932	1,839	340,5	79,8	-83,7
	18	3	12	3,8	2,70	0,696	0,464	320,5	44,3	-47,9
	19	3	12	9,5	2,70	0,564	0,175	308,6	22,1	-29,3
	20	3	12	14,9	2,70	0,189	0,109	300,2	15,2	-27,2

Day	Exp.	f (Hz)	γ (deg)	U_∞ (m/s)	Actual f (Hz)	Mean thrust (N)	St (tip)	h_0 (tip) (mm)	$\alpha_{eff,max}$ (mid) (deg)	$\alpha_{eff,min}$ (mid) (deg)
Aug 22/08										
	21	4	0	1,0	3,65	1,567	2,663	364,8	94,6	-85,9
	22	4	0	3,8	3,60	2,494	0,681	359,6	61,0	-51,8
	23	4	0	9,5	3,60	0,404	0,250	330,0	28,6	-26,1
	24	4	0	14,9	3,60	-0,020	0,149	308,3	21,3	-22,4
	25	4	3	1,0	3,60	2,853	2,719	377,7	89,7	-84,7
	26	4	3	3,8	3,60	2,997	0,669	352,9	62,5	-51,0
	27	4	3	9,5	3,65	0,415	0,252	327,5	32,6	-28,9
	28	4	3	14,9	3,65	-0,032	0,150	306,4	22,6	-24,9
	29	4	6	1,0	3,60	3,245	2,707	376,0	93,8	-86,1
	30	4	6	3,8	3,60	2,489	0,686	361,9	60,3	-51,8
	31	4	6	9,5	3,60	0,418	0,248	327,2	29,2	-28,1
	32	4	6	14,9	3,65	-0,127	0,151	308,9	23,4	-26,3
	33	4	9	1,0	3,65	3,054	2,638	361,3	90,3	-86,5
	34	4	9	3,8	3,60	1,897	0,681	359,2	60,9	-54,4
	35	4	9	9,5	3,65	0,416	0,252	327,9	30,4	-29,0
	36	4	9	14,9	3,65	-0,094	0,152	309,7	26,7	-26,5
	37	4	12	1,0	3,60	2,785	2,631	365,4	92,4	-86,5
	38	4	12	3,8	3,60	0,770	0,672	354,7	60,4	-55,7
	39	4	12	9,5	3,65	0,373	0,248	322,8	31,2	-32,1
	40	4	12	14,9	3,65	-0,166	0,150	305,9	22,4	-22,8
	41	5	0	9,5	4,50	5,363				
	42	5	0	14,9	4,50	4,239				
	43	5	3	9,5	4,55	3,923				
	44	5	3	14,9	4,55	3,407				
	45	5	6	9,5	4,55	3,188				
	46	5	6	14,9	4,55	2,143				
	47	5	9	9,5	4,55	2,263				
	48	5	9	14,9	4,50	0,697				
	49	5	12	9,5	4,55	1,220				
	50	5	12	14,9	4,50	0,040				
	51	6	0	14,9	5,10	3,246				
	52	6	3	14,9	5,15	1,418				
	53	6	6	14,9	5,20	1,291				
	54	6	9	14,9	5,25	0,379				
	55	6	12	14,9	5,25	0,414				

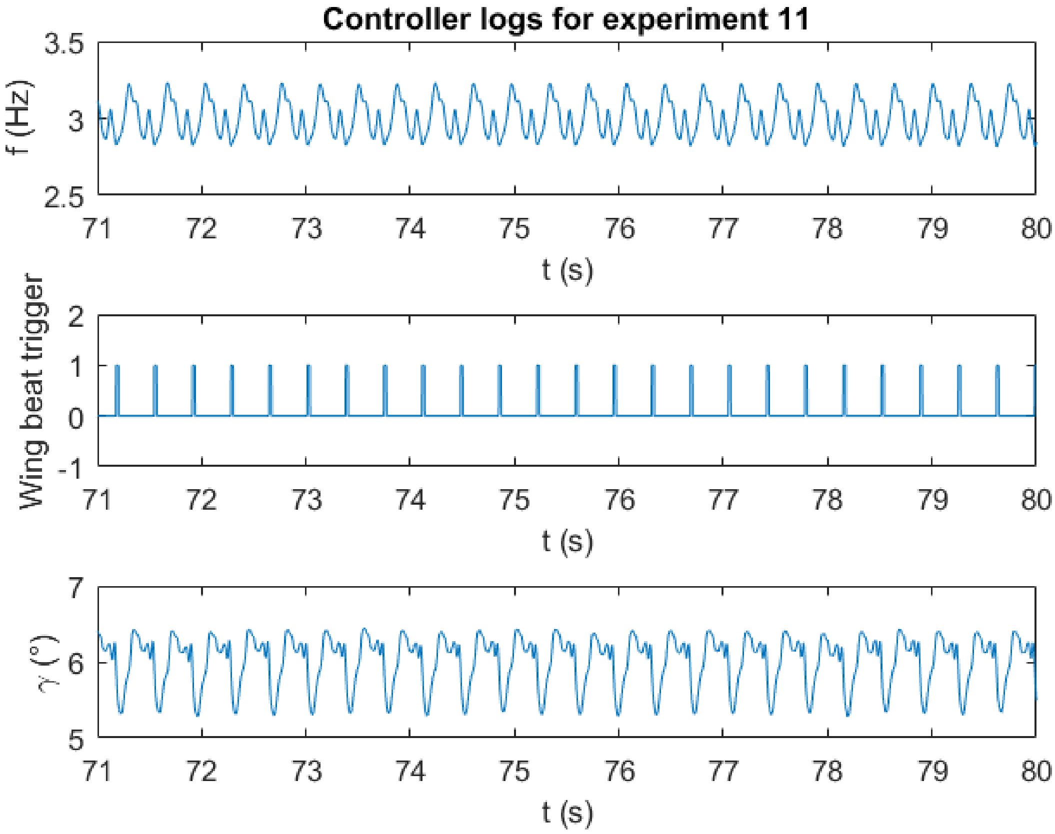

Figure 13: Controller logs of one of the motors for experiment 11. Due to the non-linear dynamics of the wing, the frequency and phase difference measured by the controller (computed using the encoder) show a periodic behaviour around their set values. Note also that by counting wing beat triggers and dividing by time, we can compute that $f_{actual} \approx \frac{24.5}{9} \approx 2.7Hz$.

Appendix D: PIV measurements

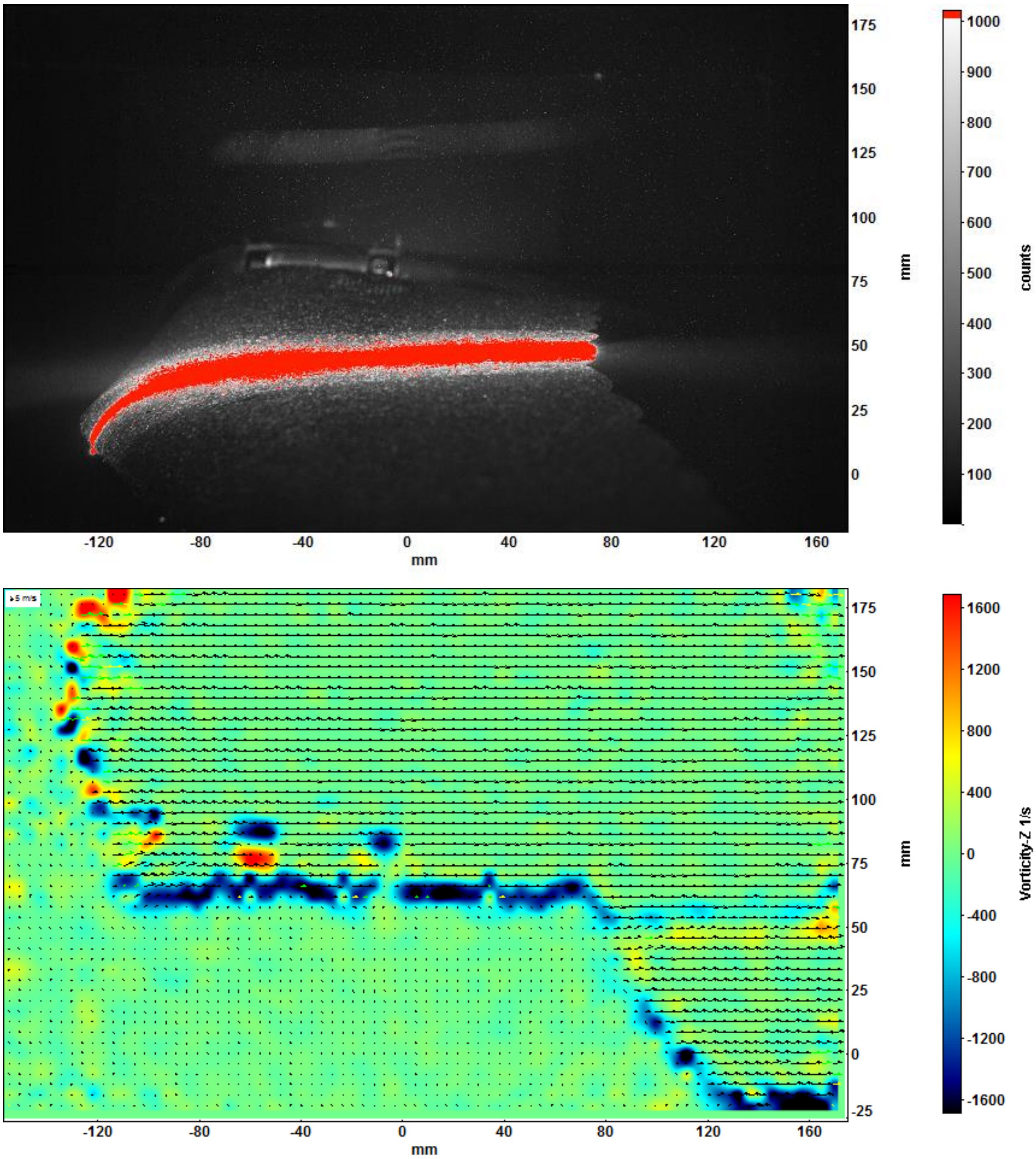

Figure 14: Raw image (top) and Z-vorticity map (bottom) for the mid-wing section during downstroke at at $f = 2$ Hz, $U_\infty \approx 14.9$ m/s and $\gamma = 0°$. Blue is clockwise, red is counter-clockwise.

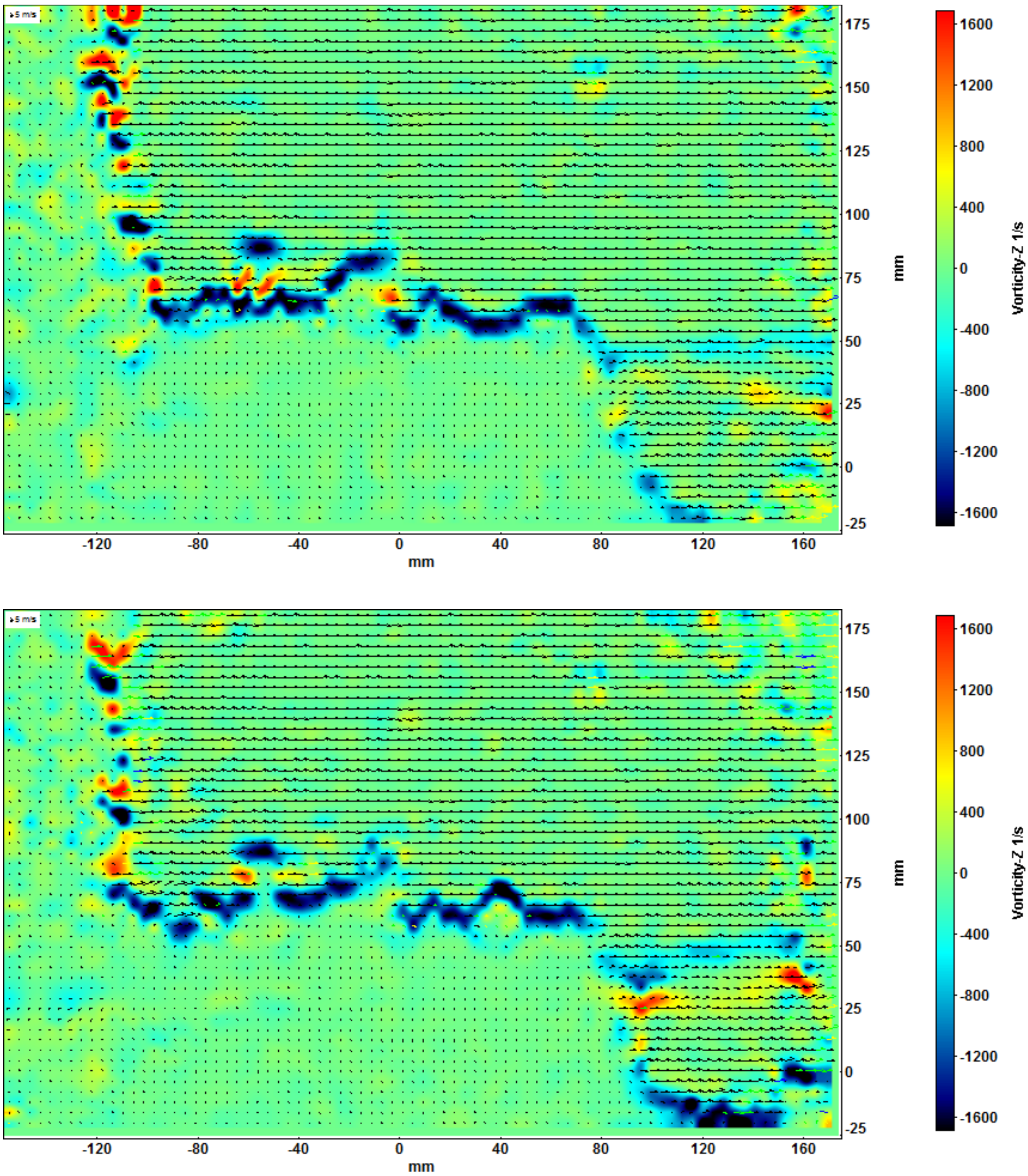

Figure 15: Z-vorticity maps for the mid-wing section during downstroke at $f = 2$ *Hz and* $U_\infty \approx 14.9$ *m/s. Top:* $\gamma = 0°$*, bottom:* $\gamma = 10°$*. Blue is clockwise, red is counter-clockwise. The second image shows increased vorticity in the wake directly behind the trailing edge.*

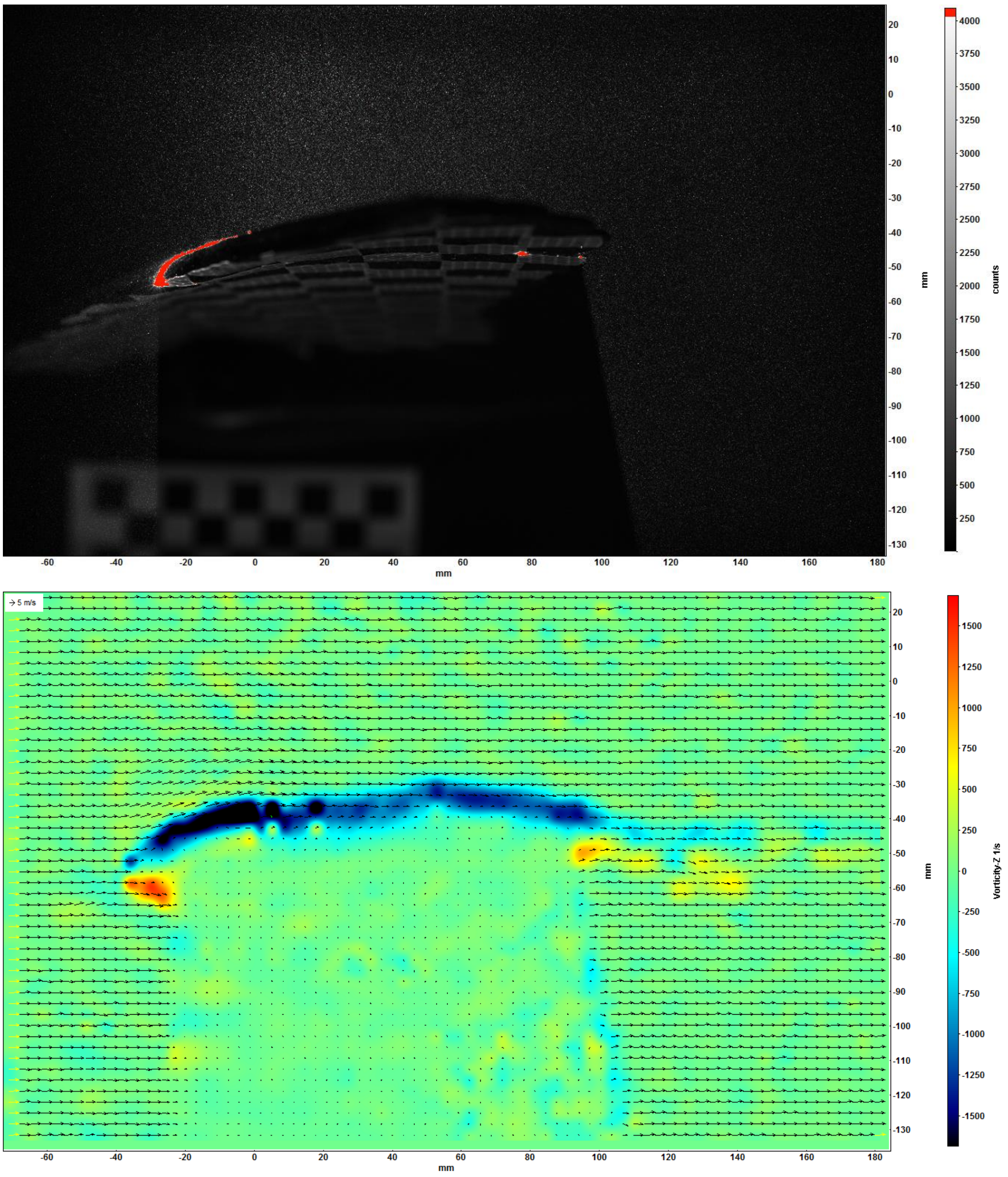

Figure 16: Raw image (top) and Z-vorticity map (bottom) for the tip section of the wing at $f = 0$ Hz, $\gamma = 0°$ and $U_\infty \approx 14.9$ m/s. Blue is clockwise, red is counter-clockwise.

Bibliography

Anderson, J. (1998). Oscillating foils of high propulsive efficiency. *J. Fluid Mech. vol 360*, 41-72.

Hover, F. (2004). Effect of angle of attack profiles in flapping foil propulsion. *Journal of Fluids and Structures 19*, 37-47.

Mulder, J. (2013). *Towards the Understanding of Flapping Wing Propulsion.*

Peyre, G. (2008). *Toolbox Graph*. Retrieved from Matlab Central File Exchange: https://nl.mathworks.com/matlabcentral/fileexchange/5355-toolbox-graph

Read, D. (2003). Forces on oscillating foils for propulsion and maneuvering. *Journal of Fluids and Structures 17*, 163-183.

Schouveiler, L. (2005). Performance of flapping foil propulsion. *Journal of Fluids and Structures 20*, 949-959.

Taylor, G. (2003). Flying and swimming animals cruise at a Strouhal number tuned for high power efficiency. *Nature vol. 425*, 707-711.

van de Ridder, L. W. (2016). *3D Motion Estimation Of A Robotic Bird Wing.*

van der Grinten, B. A. (2015). *Port based Hamiltonian modelling of flapping wing aeroelasticity using vacuum cahmber and wind tunnel measurements.*

Vaseur, C. (2014). *Robird Wind Tunnel Test Setup Design.*